LA-UR-15-24262 (Accepted Manuscript)

A geochemical approach to constraining the formation of glassy fallout debris from nuclear tests

Bonamici, Chloe Elizabeth
Kinman, William Scott
Fournelle, John H
Zimmer, Mindy
Pollington, Anthony Douglas
Rector, Kirk D.

To be published in: Contributions to Mineralogy and Petrology

DOI to publisher's version: 10.1007/s00410-016-1320-2

Permalink to record: http://permalink.lanl.gov/object/view?what=info:lanl-repo/lareport/LA-UR-15-24262

A geochemical approach to constraining the formation of glassy fallout debris from nuclear tests

Chloë E. Bonamici[1a*], William S. Kinman[1], John H. Fournelle[2], Mindy M. Zimmer[1b], Anthony D. Pollington[1], Kirk D. Rector[3]

[1]Nuclear and Radiochemistry Group, Chemistry Division, Los Alamos National Laboratory, P.O. Box 1663 MS J514, Los Alamos, NM 87545

[2]Department of Geoscience, University of Wisconsin-Madison, 1215 W. Dayton St., Madison, WI 53706

[3]Physical Chemistry and Applied Spectroscopy Group, Chemistry Division, Los Alamos National Laboratory, P.O. Box 1663 MS J567, Los Alamos, NM 87545

Abstract

Glassy nuclear fallout debris from near-surface nuclear tests is fundamentally reprocessed earth material. A geochemical approach to analysis of glassy fallout is uniquely suited to determine the means of reprocessing and shed light on the mechanisms of fallout formation. An improved understanding of fallout formation is of interest both for its potential to guide post-detonation nuclear forensic investigations and in the context of possible affinities between glassy debris and other glasses generated by high-energy natural events, such as meteorite impacts and lightning strikes. This study presents a large major-element compositional dataset for glasses within aerodynamic fallout from the Trinity nuclear test ("trinitite") and a geochemically based analysis of the glass compositional trends. Silica-rich and alkali-rich trinitite glasses show compositions and textures consistent with formation through melting of individual mineral grains – quartz and alkali feldspar, respectively - from the test-site sediment. The volumetrically dominant glass phase – called the CaMgFe glass – shows extreme major-element compositional variability. Compositional trends in the CaMgFe glass are most consistent with formation through volatility-controlled condensation from compositionally heterogeneous plasma. Radioactivity occurs only in CaMgFe glass, indicating that co-condensation of evaporated bulk ground material and trace device material was the main mechanism of radioisotope incorporation into trinitite. CaMgFe trinitite glasses overlap compositionally with basalts, rhyolites, fulgurites, tektites, and microtektites but display greater compositional diversity than all of these naturally formed glasses. Indeed, the most refractory CaMgFe glasses compositionally resemble early solar-system condensates – specifically, CAIs.

*Corresponding author
[a] Current address: Department of Earth and Environmental Science, New Mexico Tech, 801 Leroy Place, Socorro, NM 87801; ph: 1 575 835 5415; fax: 1 575 835 6436
[b]Current address: Pacific Northwest National Laboratory, P.O. Box 999 MS J4-70, 902 Battelle Blvd., Richland, WA 99352

1. Introduction

For more than 50 years, nuclear physicists and radiochemists have sought to understand the phenomenology of the nuclear fireball as recorded in the chemical and isotopic composition of glassy fallout debris (Stewart 1956; Adams et al. 1960; Freiling 1961; Freiling et al. 1965), motivated largely by forensic investigation of nuclear weapons (e.g., Mayer et al. 2013). Much effort has been dedicated to identifying bomb-derived trace components within glassy debris (e.g., Wallace et al. 2013), but there has been less systematic evaluation of natural components caught up in nuclear explosions (e.g., Eby et al. 2015). In fact, the majority (by both mass and volume) of glassy fallout debris from near-surface and underground explosions is reprocessed earth material. Thus, a geochemically based analysis of glassy debris is a potentially powerful approach to address long-standing questions about how fallout forms. Moreover, the variety of glasses produced in nature – volcanic glasses, buchites, fulgurites, meteorite-impact glasses – provide geochemists with several well-characterized analogues to aid in linking geochemical data and patterns to specific glass-forming processes.

The occurrence of trinitite, a greenish glass covering the ground surface up to ~160 m radially around the bomb detonation point, was one of several unexpected side effects of the first nuclear test on July 16, 1945. Since that time, trinitite and other detonation-formed glasses have garnered attention as long-lived products of nuclear explosions and thus for their potential value as nuclear forensic materials (Belloni et al. 2011; Bellucci et al. 2014; Bunch et al. 2012; Cassata et al. 2014; Eby et al. 2010; Eppich et al. 2014; Fahey et al. 2010; Hanson et al. 2016; Koeman et al. 2013; Lewis et al. 2015; Parekh et al. 2006; Pittauerová et al. 2010; Sharp et al. 2014; Wallace et al. 2013). Trinitite is the most accessible nuclear-explosion-formed glass and is available to non-government entities. As such, its chemical and isotopic composition has been studied extensively. Most studies of trinitite have focused on identifying trace elemental and isotopic signatures of the Trinity device within the glass matrix (Belloni et al. 2011; Bellucci et al. 2014; Bellucci and Simonetti 2012; Eby et al. 2015; Fahey et al. 2010; Koeman et al. 2013; Sharp et al. 2014; Wallace et al. 2013); backing out physical parameters of the explosion (Atkatz and Bragg 1995; Hanson et al. 2016; Hermes and Strickfaden 2005; Schlauf et al. 1997); or on assessing the long-term radioactive contamination associated with the glass (Parekh et al. 2006; Pittauerová et al. 2010).

The focus of this study is on identifying physical and chemical processes that occurred within the nuclear fireball, as recorded in the major-element chemistry of the glasses. Several recent studies have reported major-element data for trinitite and noted significant compositional heterogeneity, even at fine spatial scales (Bellucci et al. 2014; Eby et al. 2010; Eby et al. 2015; Fahey et al. 2010; Koemen et al.

2013; Sharp et al. 2014; Wallace et al. 2013). The prevailing interpretation amongst these microanalysis-based studies is that major-element compositional heterogeneity reflects partial melting ± evaporation of the Trinity test site sediment. However, major-element data have as yet to be fully integrated with or used to constrain models of fireball development and fallout formation.

Previous workers have proposed or implied a variety of conceptual models for fallout formation (Adams et al. 1960; Belloni et al. 2011; Freiling et al. 1965; Glasstone and Dolan 1977; Hermes and Strickfaden 2005; Miller 1960). In general, these models invoke fallout particle growth in the fireball by condensation of compositionally fractionated melts as independent droplets or around nuclei of ground material, followed by partial or complete compositional homogenization while particles are still at least partially molten (Adams et al. 1960; Glasstone and Dolan 1977; Izrael 2002; Miller 1960). These models therefore predict a homogeneous or weakly layered isotopic composition, such that an aerodynamic particle is effectively a single, averaged sample of the various compositionally fractionated environments through which it passed.

Existing models largely agree on the broad features of fallout formation, yet, in detail, differ in the stated or implied mechanism of device-material (radionuclide) incorporation into macroscopic debris. In the case of surface or near-surface detonations, the majority of fallout is made up of explosion-processed ground materials; the device and any detonation structure (a steel tower in the case of Trinity) represent very small contributions to the overall mass of the debris (Freiling et al. 1965; Stewart 1956). While many studies propose that at least some of the ground material vaporizes along with the device during the explosion (e.g., Belloni et al. 2011; Bellucci et al. 2014; Freiling et al. 1965; Glasstone and Dolan 1977; Izrael 2002), the majority of ground material is thought to participate in fallout formation as molten or even unmelted solid particles (Adams et al., 1960; Eby et al., 2015; Glasstone and Dolan 1977; Hermes and Strickfaden 2005; Lewis et al. 2015; Miller 1960). It is generally assumed that the materials that derive from the device - metals, actinide-based fuel, and fission products (and/or their oxides) - are among the most refractory constituents involved in a detonation, and thus, that they become highly concentrated within molten condensates (Adams et al. 1960; Freiling et al. 1965; Miller 1960; Stewart 1956), which form as micrometer-scale liquid particles or as thin liquid layers on ground-material nuclei. On the basis of equilibrium condensation calculations and classical nucleation theory, it has been argued that there is insufficient time during cooling of the fireball to condense particles with radii larger than ~20 μm (Stewart 1956), and thus in order to form macroscopic radioactive fallout, device constituents must combine in some way with bulkier ground materials. Some workers have postulated radionuclide incorporation by direct diffusive exchange between radionuclide-

bearing vapor and molten ground material droplets (Freiling et al. 1965). Others have proposed condensation of thin layers of radionuclides-enriched melts onto ground-derived molten particles, followed either by diffusive exchange of radionuclides between the melts, or a combination of diffusion and physical mixing of liquid condensate and liquid ground materials (Adams et al. 1960). At later times and lower overall temperatures, radionuclide-enriched condensates may also be deposited onto solid ground particles and remain as unhomogenized radioactive coatings on macroscopic fallout particle surfaces (Miller 1960).

This study undertakes detailed characterization of the major-element composition of Trinity glasses and their relationship to radioactivity within aerodynamic trinitite debris. We show that some glass phases formed by melting of individual minerals and/or mineral aggregates but that the volumetrically dominant glass phase in aerodynamic trinitite beads likely formed, in its entirety, by condensation. Textural relations between the different fallout phases and chemical trends within the main glass phase provide a basis for constructing a relative chronology and updated model for the formation of macroscopic glassy nuclear fallout.

2. Site geology and samples

The major-element chemistry of the glasses derives from the test-site substrate, which contributed the bulk of the material that was ultimately entrained within the fireball. The Trinity device was detonated from atop a 30-m steel tower and produced a shallow, irregular crater – approximately 340 m in diameter, with a maximum depth of 2.9 m – through a combination of excavation and compaction (Reines et al. 1945). Based on pre- and post-test surveys of the site, Reines et al. (1945) calculated that about 30% of the total crater volume (1.1×10^4 m^3 of the total 3.7×10^4 m^3) could be attributed to excavation of the substrate. Thus, 1.1×10^4 m^3 is the best estimate for the volume of test-site sediment entrained within the fireball.

The Trinity Site is located ~75 m above the Jornada del Muerto basin floor on distal alluvial fan deposits of the Oscura Mountain range, which rises 5 km to the east (Fig 1A, B). A well drilled at the Trinity tower location prior to tower construction logged “sand and gravel” to a depth of at least 55 m (Reines et al. 1945). The sediment of the test site is a poorly sorted arkose to lithic arkose (Eby et al. 2010; Koeman et al., 2013; Ross 1948; this study) comprising primarily alkali feldspar, sodic plagioclase, quartz, and limestone fragments derived from the weathering of the Mesoproterozoic granitoids and Pennsylvanian limestones exposed in the Oscura Mountains (Fig. 1 C-G). Rarely, fragments of chert and sandstone are also observed. Fahey et al. (2010) proposed an exhaustive list of potential sediment constituents based on previous studies of atmospheric dust over the White Sands Missile Range and the

Tularosa basin evaporite deposits 55 miles south of the test site; however, this study finds no evidence of eolian or evaporite deposits currently at the test site. Accordingly, we suggest that the test-site sediment composition reflects primarily local erosional products of the Oscura Mountains, with minimal contributions from distant playa deposits.

Samples of fallout debris selected for this study are spheroidal beads, whose rounded shapes indicate that they were molten and airborne during the explosion but solidified prior to falling to the ground surface. In other words, aerodynamic trinitite is nuclear fallout *sensu stricto*. These samples contrast with samples of previous studies, which have almost exclusively analyzed flattened, amorphous trinitite crusts (sometimes also called "pancake trinitite"). Trinitite crusts may have formed as in situ ground melts (Parekh et al. 2006) or by puddling of molten material rained out of the nuclear cloud (Belloni et al., 2011; Hermes and Strickfaden 2005) or some combination of both. Aerodynamic beads unambiguously interacted with the nuclear fireball, and thus their compositions are more directly related to fireball processes.

Eleven pieces of morphologically aerodynamic trinitite were selected from an archived collection of Trinity test debris housed at Los Alamos National Laboratory. Debris pieces were 4-10 mm in diameter, opaque, and pale to deep green-brown; several displayed an iridescent vitreous luster over at least part of their surfaces (Fig. 2). Pieces 8768-4, -5, -10, and -12 were single spheroids with smooth, unbroken exteriors, whereas pieces 8768-6, -7, -8, -14 were lumpy single spheroids with visible vesicles. Debris pieces 8768-9, -11, and -13 were composite objects made up of two or more single beads or bead fragments. Debris pieces were sectioned and cast into 26-mm diameter round epoxy mounts along with multiple standard reference glasses. Several pieces of debris broke into smaller fragments during sectioning and only fragments were mounted. Bead interiors were exposed in cross-section at the mount surfaces (Fig. 2), which were polished to 1-µm relief through a series of alumina lapping films and diamond-grit suspensions. Samples were cleaned following preparation and between each type of analysis with multiple sonications in de-ionized water and ethanol.

3. Methods

3.1 SEM imaging and phase maps

Sample mounts were gold- or carbon-coated, imaged using backscatter electron detection, and mapped by energy dispersive spectroscopy (EDS) on an FEI Quanta™ 200F field-emission gun scanning electron microscope, equipped with an EDAX Apollo 40 EDS detector, at Los Alamos National Laboratory. Maps were collected by scanning with 15-keV accelerating voltage and a 4-µm-diameter beam over a 512 x 400 pixel region at 30-50x magnification (depending on the size of the piece of

trinitite). Dwell time per pixel was 200 or 400 µs, and amplifier response time was set to 12.6 or 21 ns to produce ~20-40% dead time.

Debris samples were too large to be mapped in a single scanned area, so sectors of the debris were mapped and the maps subsequently stitched together with Adobe Illustrator software. Due to image aberrations, especially near image edges, some images have been slightly digitally distorted in order to align smoothly with neighboring images. Small variations in the field emission-source coherency and chamber pressure from day-to-day resulted in the observed minor variations in spectral intensity between mapped quadrants of the same piece of debris.

Phase maps were constructed by assigning three element maps to RGB channels with EDAX spectral analysis software. Several combinations of elements were tested, and those displaying the clearest and most relevant compositional variations are shown in Figure 3. Variations in spectral intensity between mapped quadrants within a piece of debris were compensated for by differential scaling of channel intensities in the RGB mixed image. Because phase maps are qualitative and used only to assess compositional variations in the context of textures, this type of scaling does not affect interpretations.

3.2 Digital autoradiography

Sample mounts containing the trinitite beads were cleaned and sealed inside a FujiFilm BAS TR2025 cassette (25-µm spatial resolution) facing an image plate for 8.5 days. The image plate was digitally developed with a GE-Healthcare Typhoon FLA-7000 laser scanner.

Haloes of apparent activity extending into the epoxy from around the trinitite beads indicate that “bleed-over” of the activity signal occurred as a result of overexposure of the image plate. This suggests that the size of activity domains is slightly exaggerated on the autoradiograph image relative to the true size of the active domains with the pieces of debris. We applied a combination of image brightness reduction and contrast enhancement to mitigate these bleed over effects. The appropriate degree of brightness/contrast adjustment was gauged by reduction of the halo around a piece of debris and by comparing uniquely shaped activity domains with the shapes of glass domains as imaged by SEM backscatter. Because the activity occurs only in the CaMgFe glass (see section 4.2), determination of the appropriate brightness/contrast scaling adjustment and alignment of the activity and SEM images were straightforward.

3.3 Electron microprobe analysis

Quantitative wave-length dispersive spectroscopy (WDS) compositional measurements were performed at the University of Wisconsin-Madison on a Cameca SX-51 electron microprobe. Data

collection and reduction were performed with Probe For EPMA software, version 10.4 (Donovan 2016). Samples were either carbon- or iridium-coated (see section 4.3), and either nine or ten elements were measured – O, Na, Mg, Al, Si, K, Ca, Ti, Fe, and sometimes C – with a 15 keV accelerating voltage and 10 nA beam current. The beam was defocused to a 10-μm spot size and all measurements were collected with time-dependent intensity (TDI) recording in order to correct for loss of alkali elements to beam-induced volatilization during the analyses (Lineweaver, 1963; Morgan and London 1996). The defocused beam, however, proved sufficient to prevent sample beam damage and alkali loss, and TDI corrections were ultimately not applied. All elements were measured with 10-second on-peak counting times and 5-second off-peak background counting times, except oxygen, which was measured with 20-second on-peak and 10-second off-peak background counting times. Background correction schemes differed depending on the element: Na, Ca, K, and Ti raw counts were corrected by linear interpolation between selected high and low background positions; Mg, Si, Al, and Fe were corrected by averaging high and low background position counts; and O was corrected with a user-defined, multipoint exponential background fit. Unknown trinitite glasses were investigated for the potential presence of additional elements by WDS scans. Elements N, F, P, S, Cl, Cr, Cu, Eu, Pb, Sr, Zr, Mo, Cs, Ba, U, and Pu were below detection for EPMA. A small amount of Mn, at the level of ~0.1-0.2 element weight percent, was present in some Ca-rich trinitite glasses.

All elements, except Ti, were calibrated by measurements on well-characterized standard glasses - rhyolite obsidian MM-3 (Na, K, O), NBS standard reference glass K411 (Mg, Ca, Si, Fe, O), NBS standard reference glass K412 (Al, O), and an in-house high-purity silica glass (Si, O). Titanium was calibrated on a synthetic rutile standard developed at the University of Wisconsin. Following initial peaking and calibration on standard and unknown trinitite glasses, the MM-3, K411, K412 and high-purity silica glass standards were re-run every ~4-8 analysis hours to monitor and correct for instrumental drift.

3.4 Laser Raman spectroscopy

Five locations in two pieces of debris were investigated with confocal laser Raman spectroscopy using a Witec Alpha 300 AFM/Raman/SNOM microscope. Single spectra were collected by excitation of a ~1-2 μm^3 sample volume using a 10-20 mW doubled Nd-YAG laser operating at 532-nm and focused through the 20x objective of the optical microscope. All analyses employed a 600-grooves/mm (BLZ 500 nm) diffraction grating centered at 600 nm. Integration times were typically 0.5-2.0 s for 50-100 co-added accumulations in a thermoelectrically cooled (-60 °C) EMCCD with preamplifier gain set to 1. No background subtractions or other corrections have been applied to the spectra.

4. Results

4.1 SEM imaging and phase maps

Backscatter electron imaging and phase maps constructed from EDS element maps show multiple texturally and chemically distinct domains within trinitite beads (Fig. 3; Supplemental Materials 2). Phase maps delineate three glass types with distinctly different compositions – an essentially pure silica glass, a glass rich in alkali elements K and Na, and a glass characteristically containing Ca, Mg, and Fe – in addition to mineral fragments and clumps. Beads that are macroscopically smooth and spheroidal comprise disseminated blebs of alkali and silica glass and/or quartz fragments encased within the CaMgFe glass (Fig. 3: #4,5,10,11,12). EDS mapping does not allow for differentiation of crystalline quartz from amorphous silica glass; however, textural features provide evidence that both are present. Beads that are macroscopically lumpy and vesicular (Fig. 3: #6,7,11,13,14) comprise mineral aggregates and/or pods of frothy silica glass encased within a thin rind of CaMgFe glass, which contains the same assemblage of disseminated glass and mineral inclusions that appear in the smooth beads. Grain boundaries between minerals in minerals aggregates are filled with a vesicular, amorphous, Ca-rich glass phase that locally exhibits <10 μm crystallites. No crystallites are observed in any other glass phase.

The included phases are approximately equidimensional and exhibit sharp to slightly gradational contacts with the surrounding CaMgFe host glass. Silica domains inferred to be crystalline quartz fragments are angular and commonly display fracture. Silica domains inferred to be glass show a complete textural gradation from subangular or subrounded domains with rare vesicles aligned along domain boundaries to irregular pods of highly vesicular froth. Alkali glass consistently appears as rounded, moderately to highly vesicular blebs. BSE images and phase maps show that the CaMgFe glass is compositionally heterogeneous and that different compositional domains within the phase commonly appear as elongate lenses, stringers, and layers. Many regions of CaMgFe glass display incipient compositional banding deflected or wrapped around included phases and vesicles (Fig. 3: #4,9,12).

4.2 Activity maps

Autoradiographs of trinitite beads reveal the spatial distribution of α and β radiation-producing isotopes. Energetic γ rays typically pass through the image plate without interacting with the radiography film and are therefore not well-represented in autoradiography maps.

Digital autoradiography maps of trinitite beads show that radioactivity is confined to the CaMgFe glass (Fig. 3). Mineral fragments, mineral aggregates, silica glass, and alkali glass show no activity. What is more, the distribution of radioactivity in the CaMgFe glass is patchy. There are no clear spatial relationships or organized patterns of zoning (e.g., coherent core-to-rim activity variations)

within a given piece of debris. There is no clear correlation between autoradiograph intensity and backscatter intensity or measured elemental abundances within the CaMgFe glass.

4.3 Electron microprobe data

Electron microprobe measurements confirm the presence of a nearly pure silica glass, an alkali-rich silicate glass, and a CaMgFe silicate glass. All EPMA data are tabulated in Supplemental Materials 1 and the locations of all analysis points are mapped in Supplemental Materials 2.

Alkali glasses in trinitite samples have a restricted range of elemental abundances (Fig. 4A) – e.g., Si (29-32.5 elem. wt.%) and Al (9.5-13 elem. wt.%), high alkalis (Na+K = 8.5-16 elem. wt.%), and low Ca (0-3 elem. wt.%). Elemental abundance and proportions in alkali glass are nearly identical to elemental abundances and proportions in crystalline feldspars found in melt-cemented mineral aggregates within some beads (Fig 3B). Two distinct alkali glass compositions corresponding to two distinct feldspar compositions are present – a K-rich (sanidine) composition and a Na-rich (andesine) composition (Fig. 4). A small number of alkali glass analyses fall between these two endmember compositions.

The CaMgFe glass is the volumetrically dominant glass phase present in the trinitite beads examined in this study. While it characteristically contains Ca, Mg, and Fe, it shows significant variability in these and all other major and minor elements (Fig. 4B). Minor elements, Mg, Fe, and Ti, show the least variability, whereas major elements, Ca, Al, and Si, show the greatest variability. Generally, beads containing only a few texturally distinct domains (Fig. 3: #10, 13) show less compositional variability than beads containing many texturally distinct domains (all others). Binary plots show at best moderately developed correlations between element abundances (Fig. 5A); in general, a broad covariance – positive or negative – is discernible, but in detail the correlations are not strong.

Initially, many measurements, especially of CaMgFe glass, yielded low analytical totals, between 96-98 wt.%. This is consistent with results from previous semi-quantitative (EDS) studies of trinitite glass (Eby et al. 2010; Eby et al. 2015; Fahey et al. 2010) and two previous quantitative (WDS) studies of trinitite glass (Bellucci et al. 2014; Sharp et al. 2014). Wavescans ruled out the presence of unmeasured elements as a cause of low totals; however, carbon was not measured in the first analytical session because of the use of a carbon coat for sample conductivity. A second analytical session with iridium-coated samples and including carbon as an analyzed element, revealed that most CaMgFe glasses, with a few exceptions, do not contain detectable carbon. Nonetheless, weight percent totals improved when carbon was measured rather than assumed (uniform carbon coat thickness). This suggests that absorption of O and Si X-rays in glasses is very sensitive to carbon abundance and that even small

variations in carbon, probably arising from carbonaceous surface contamination, can affect calculated elemental totals.

4.4. Laser Raman spectra

All five spectra from beads #4 and #14 yielded broad peaks in the 200-1200 cm^{-1} range (Fig. 6), typical for silicate glasses that contain predominantly oxygen-bonded metallic cations (e.g., Mysen and Pascal 2005). The broad peaks at low wavenumbers are convolutions of several individual peaks, including those arising from M-O bond stretching in Si or Al tetrahedra, vibrations within silicate ring structures, and vibration of intra-network cations (e.g., Morizet et al. 2012). Less typical for silicate glasses, three of the trinitite spectra show distinct peaks above 1250 cm^{-1}. One spectrum in bead #4 shows a pair of peaks, at 1350 cm^{-1} and 1580 cm^{-1}, that are consistent with the G and D bands of graphite (Fig. 6, spectrum 4). One spectrum from Si-poor glass in bead #14 contains a peak doublet with similar intensities and spacing but shifted down by approximately 90 cm^{-1} relative to the typical G and D graphite band locations (Fig. 6, spectrum 2). Another spectrum from Si-richer glass in bead #14 contains a series of small peaks at 1300 cm^{-1}, 1430 cm^{-1} and 2850-3030 cm^{-1} (Fig. 6, spectrum 5), which are characteristic of stretching and bending modes of the aliphatic CH_2 and/or CH_3 molecular groups.

5. Discussion

5.1 Melting vs. condensation

Previous authors have variously attributed fallout glasses to melting (e.g., Eby et al. 2015; Lewis et al. 2015) and/or to condensation (e.g., Izrael 2002; Freiling et al. 1965). The distinction is nontrivial for the interpretation of chemical and isotopic signatures. Compositional data of this study suggest that trinitite silica and alkali glasses are melting products, whereas the trinitite CaMgFe glass formed by condensation of evaporated ground, structure, and device materials.

Silica and alkali glasses have compositions that are directly equivalent to mineral constituents in the substrate sediment (Fig. 4A; Supplemental Materials 1), as would be expected for glasses formed by melting individual sand grains. Textural variations of silica glasses are consistent with various stages along the solid-to-melt-to-vapor transition. Unmelted quartz grains appear in debris as angular, fractured fragments. Partially melted quartz grains appear as subangular or subrounded fragments with slightly gradational boundaries and a few, small vesicles concentrated near the grain boundaries (Fig. 3: #4). Wholly melted quartz occurs within trinitite as rounded silica blebs with disseminated vesicles (Fig. 3: #4-12). Highly vesicular (frothy) amorphous silica - hereafter referred to as lechatelierite (Fig. 3: #9,14) – indicate silica melts near the boiling point. Alkali glass domains show less textural variability than silica

glass domains; they are always subrounded to rounded, moderately vesicular domains suggestive of full melting.

In contrast to the alkali and silica glasses, CaMgFe glass compositions vary widely from bead to bead and within individual beads (Fig. 4; Supplemental Materials 1). On a total-alkali silica diagram (Fig. 7), CaMgFe compositions span and surpass the SiO_2 range of terrestrial silicate magmatic rocks. Very broadly, interelemental trends (Fig. 5) can be interpreted in terms of covariation in the abundances of constituent minerals in the bulk sediment – i.e., elements that derive predominantly from the same mineral are positively correlated, whereas elements that derive predominantly from different minerals are negatively correlated. For instance, CaO and Al_2O_3 are negatively correlated with SiO_2 and each other (Fig. 5), presumably because the main sources of Ca, Al, and Si were calcite, feldspar, and quartz, respectively. In detail, however, most of these correlations are not linear and show significant scatter – as reflected in generally low correlation coefficients (Fig. 5A). Principal components analysis (PCA) also distinguishes the anticorrelation between the main elemental constituents in calcite (CaO), feldspar (Al_2O_3), and quartz (SiO_2) but shows poor dispersion of most of the analyses (Fig 5B). Furthermore, PCA demonstrates anticorrelation of Na_2O and K_2O with Al_2O_3, indicating that variation in these elements is not simply controlled by feldspar abundance.

Melting phenomena acting in the bulk test site sediment (not on dispersed individual grains) that might produce the trinitite glasses can be circumscribed by three scenarios. The first scenario is equilibrium partial melting of the test site sediment, followed by melt mixing. Equilibrium melting of multiphase materials occurs via heterogeneous reactions rather than by fusion of individual phases, and melt compositions are thus constrained by multiphase eutectic equilibria (e.g., Winter 2014). Consequently, equilibrium partial melting of continental crustal rocks, including sedimentary rock equivalents of Trinity site sediments, produces a limited range of melt compositions – typically andesitic to rhyolitic (e.g., Montel and Vielzeuf 1997; Thompson 1982; Vielzeuf and Holloway 1988). Mixing of intermediate to felsic melts could not produce SiO_2-poor trinitite melts. In addition, for reasons discussed in a section 5.2.1, it is unlikely that mixing was an efficient process in the trinitite melts. A second melting scenario involving selective and/or largely incongruent melting of individual minerals within the bulk sediment (i.e., strongly disequilibrium melting) could generate a wider range of compositions. Disequilibrium melting implies thermal disequilibrium and temperature heterogeneity at the scale of individual mineral grains, a condition that may develop in cases of spatially focused or directional heating, as through electrical currents (e.g., lightning strike), but that is unlikely to develop as a result of radiant (gamma-ray induced) heating within the sphere of a nuclear blast. The third scenario

is wholesale melting of a sediment that itself spanned the entire range of observed glass compositions. While natural sediments can be heterogeneous as a result of disparate sources and/or depositional environments, these are well constrained for the Trinity site by modern observations (see section 2). There is little evidence to suggest that the test site sediment composition varied drastically within the 2-3 m excavated by the Trinity blast.

These melting scenarios either cannot explain the observed trinitite glass compositional variability (equilibrium melting) or are improbable given the dynamics and environment of the Trinity explosion (disequilibrium melting, extremely heterogeneous sediment). A more reasonable process for generating the large CaMgFe glass compositional variability is bulk sediment evaporation and elemental fractionation during subsequent condensation to melt. Volatility-controlled condensation from a vapor should produce a sequence of refractory-element-enriched to volatile-element-enriched condensates that have both higher and lower abundances of each element than the vapor from which they condensed.

In order to test a condensation hypothesis compositional variations in the trinitite glasses must be assessed relative to the bulk ground material from which they were derived. Thus, the starting composition of the test-site sediment must be constrained. We were unable to locate any published or unpublished bulk major-element data for pre- or post-detonation Trinity site sediment, nor are there records of the test-site sediment being sampled (or archived) for elemental analysis prior to the test. The explosion crater was backfilled following the test (Hermes and Strickfaden 2005), displacing any remaining *in situ* sediment. Furthermore, the U.S. Army, which now has stewardship of the Trinity Site as part of the White Sands Missile Range, does not permit sampling. Accordingly, we estimate the bulk composition (Table 1) based on the site geology as observed on a site tour by the authors and as mapped by state geologists (Fig. 1); descriptions of source rocks from the Oscura Mountains (Kottlowski 1953; Weber 1964); descriptions of Jornada Del Muerto basin fill (Neal et al. 1983); and the mineral modes of melt-cemented mineral aggregates embedded in aerodynamic trinitite samples of this study (Fig. 3; Supplemental Materials 3). Figure 4 shows the range of elemental abundances in all the estimated bulk compositions for comparison with measured CaMgFe glass compositions.

Relative to the calculated bulk test-site sediment compositions (Table 1), CaMgFe glasses range from enriched to depleted in all major elements (Fig. 4, 8). On average, the CaMgFe glasses are depleted in alkalis and enriched in Fe and Ca relative to a likely sedimentary precursor (Fig. 8). Alkali-depleted CaMgFe glass compositions are difficult to reconcile with partial melting of the test-site sediment, which should generate melts enriched in these incompatible elements. Although most CaMgFe glasses are

neither enriched nor depleted in the refractory element Al, some CaMgFe compositions show large Al enrichment (Fig. 8). Altogether, the span of glass compositions is consistent with a process that fractionates elements on the basis of volatility to produce melts/glasses both more and less refractory than the bulk arkosic precursor. The variability in the CaMgFe glasses is, therefore, most consistent with formation by volatility-controlled condensation from a plasma. This conclusion also explains the exclusive occurrence of radioisotopes in CaMgFe glasses, as well as the strong spatial correlation between high-activity regions and high Ca and Al content (Fig. 3): device-derived elements co-condensed with non-radioactive, environmentally derived elements.

Experiments to measure directly the temperature of the Trinity explosion failed, but estimates of temperature have been constructed from measurements of illumination over the first ten seconds of the explosion (Fig. 9; Bainbridge 1976). More information about the thermal evolution of nuclear clouds is available from theoretical calculations and subsequent, more closely monitored tests. A nuclear explosion produces temperatures in excess of 10^6-10^7 K within a millisecond in the immediate vicinity of the detonation (Glasstone and Dolan 1977). The fireball forms and expands when energy from the explosion, initially mainly in the form of X-rays, is absorbed by the surrounding air and ground materials, which are vaporized and variably ionized during the process. By the time the shock front separates from the radiation front (10-100 ms), the interior temperature of the fireball is ~4000-8000 K, which then cools to ~1500-2000 K in <10 seconds (Glasstone and Dolan 1977). Theoretical calculations of Izrael (2002) suggest that entrainment of ground debris slows cooling of the fireball, possibly by promoting isothermal phase transitions, and may allow additional time for isotopic fractionation in condensing vapor. Previous authors have assumed that evaporation was highly incongruent and affected predominantly the device and structural materials (Adams et al. 1960; Freiling et al. 1965), but it seems probable that most sand-sized geological materials experiencing temperatures in excess of 4000 K would evaporate as well. Ground materials incorporated later, and at lower temperatures, may well have experienced only partial melting or partial evaporation.

Condensation is likely to have been heterogeneous in both time and space because temperature and composition within the fireball were likely heterogeneous in time and space (Dai et al. 2013; de Niem et al. 2008; Ebel and Grossman 2005). In a gross sense, the outer surface of the fireball would be expected to cool most rapidly, and interior regions to cool more slowly (Glasstone and Dolan 1977). However, convection and turbulence are known to develop within the fireball, with their most well-known manifestation, the mushroom cloud, appearing after several seconds. Convection can segment the fireball into different thermal (and possibly compositional) regions on the scale of 10s-100s of

meters. Turbulence, while promoting finer-scale mixing, introduces and disperses additional ground material capable of inducing localized thermal and compositional gradients at the scale of micrometers to centimeters.

Geochemical evidence presented here for the formation of macroscopic volumes of CaMgFe melt through condensation is at odds with previous authors' calculations of condensed particle size (~ 20 μm; Miller 1960; Stewart 1956). This discrepancy reflects differences in the inferred condensation environment between those studies and the current work. Early theoretical calculations were based on classical homogeneous nucleation theory (Stewart 1956), where nucleation rate and melt-phase growth depend on particle encounter frequency within a diffuse-gas medium. The current study infers predominantly heterogeneous nucleation within a "dusty" (complex) plasma. More recent models of impact-formed condensates that include heterogeneous nucleation predict condensed droplet diameters one to two orders of magnitude larger than the ~20-μm diameter of classical nucleation models (Johnson and Melosh 2012; Johnson and Melosh 2014; Melosh and Vickery 1991). Furthermore, ionization can significantly enhance nucleation rates (e.g., Vishnyakov et al. 2011), though the mechanisms of enhancement are as yet debated and likely vary as function of plasma composition (e.g., Kathmann et al. 2005). Electrostatic and magnetic fields that arise in plasmas promote longer-range particle interactions and self-organization phenomena (e.g., Morfill and Ivlev 2009). In a rapidly cooling system, such phenomena could greatly enhance particle encounter rates and, thus, condensation rates (relative to condensation in an inert gas). A combination of higher nucleation rates and higher encounter frequency could allow formation of substantial condensed melt volumes, even over short time periods.

5.2 Melt interactions in trinitite

Whether melts form by a solid-to-liquid phase transition or a vapor-to-liquid phase transition, interactions between liquid phases can alter primary melt compositions. In particular, liquid-phase interactions can lead to homogenization (of both chemical and isotopic species) through convective-dispersive mixing and/or diffusion. In this section, we assess the contributions of these processes to the observed compositional variation in trinitite glasses, and especially, in the CaMgFe glass.

Melt interactions in trinitite precursors are broadly constrained to a temperature range between the upper condensation temperature of CaMgFe melts and the glass transition temperature(s), where melts become structurally and rheologically stiff – i.e., when physical and diffusive exchange processes become so slow as to be negligible in altering melt composition. Although pressures inside the fireball may reach several gigapascals immediately after detonation (Glasstone and Dolan 1977), condensation and subsequent melt interactions probably occur at circum-atmospheric or even sub-

atmospheric pressures in the wake of the outwardly migrating shockwave (Fig. 9). Equilibrium condensation calculations of Yoneda and Grossman (1995) for "dusty" (Si-enriched) systems at circum-atmospheric pressures therefore suggest an upper temperature limit for condensation, and thus for melt interactions, of ~2200 K. At the low temperature limit, viscosity modeling (see section 5.2.1 below) yields estimates of glass transition temperature (T_g) for a given melt composition (Fig. 10, inset). All calculated T_g values for alkali and CaMgFe glasses are greater than 900 K, which provides a conservative estimate of the temperature at which any melt interactions – mingling or diffusion – would have effectively ceased.

5.2.1 Viscosity - implications for melt mixing

Textural relationships and generally sharp, vesicle-lined contacts between the three distinct types of glass in trinitite beads suggest that there was physical mingling of precursor melts, but limited convective and/or dispersive physical mixing. Alkali and silica glasses occur as rounded, approximately equidimensional blebs within enveloping CaMgFe glass, a relationship indicating that precursor alkali and silica melts were highly viscous melt pods that behaved as essentially rigid objects within a lower-viscosity, fluidal CaMgFe melt matrix. In general, compositional variation within the CaMgFe glass itself is patchy, with local development of compositional banding wrapping around included phases, consistent with overall lower viscosity for CaMgFe melts and greater similarity in viscosity between different CaMgFe melts than between alkali or silica melts and CaMgFe melts.

In order to quantify texture-based inferences about viscosity, we used the model of Giordano et al. (2008) and EPMA-measured glass compositions to calculate anhydrous viscosities of CaMgFe and alkali melts in the temperature range 600-1800 K. The Giordano et al. (2008) model accommodates non-Arrhenian temperature dependence in weakly polymerized silicate melts – e.g., Si-poor melts like the more refractory CaMgFe compositions. Temperatures greater than 1800 K are beyond the calibrated range of the model, as are pure silica melt compositions. All compositions of alkali glass yield essentially identical model viscosity curves, with approximately 16 orders of magnitude variation in viscosity over the modeled temperature range. In contrast, CaMgFe glasses yield a great variety of model viscosity profiles, and generally much larger variations in viscosity over the modeled temperature range (Fig. 10). Thus, the modeling predicts a significant viscosity contrast between alkali melts and most CaMgFe melts at all temperatures between 800 K and 1800 K. In general, alkali melts are 2-5 orders of magnitude more viscous than CaMgFe melts for a given temperature. Experimentally determined viscosity of molten quartz (Fig. 10; Ryan and Blevins 1987) suggests that the viscosity of trinitite silica glasses would have been ~5-10 orders of magnitude greater than the viscosities of most CaMgFe glasses over the same

temperature range. Eby et al. (2015) calculated similar viscosity values and similar viscosity differences based on compositions of ground crust trinitite glasses. Such large viscosity contrasts would inhibit melt mixing (e.g., Huppert et al. 1984). We conclude that melt mixing was not an efficient process within trinitite debris and therefore could not have acted to significantly homogenize melt chemical or isotopic composition.

5.2.2 Diffusion

Electron microprobe traverses across contacts between different types of glass within trinitite beads show element concentration gradients consistent with limited diffusive exchange of major and minor elements between melts (Fig. 11). Concentration gradients have an inflection point centered at the glass-glass contact and nearly symmetrical or somewhat asymmetric shoulders extending into concentration plateaus on either side of the contact. Diffusion profiles are best developed for Si, Ca, and Al. Distances for 90% exchange of these low-diffusivity elements are 10-30 µm. Where alkali-rich glass contacts alkali-poor glass, diffusion profiles are also developed for Na and K, but the 90% exchange distances for these elements is consistently greater (~20-50 µm) than for non-alkali elements.

Assuming that the duration of melt presence (period between initial condensation and glass transition) within the fireball can be approximated by the duration of diffusive exchange between melts in fallout beads, we performed diffusion modeling of Si profiles across selected glass contacts. The six modeled profile segments span contacts between glasses with differences of 4 to 12 Si element wt.% – either CaMgFe and alkali glass contacts or high- vs. low-Si CaMgFe glass contacts. Features, especially asymmetric profile shoulders, of some profiles suggest that multicomponent diffusion occurred (Fig. 11E); however, because it is very difficult to construct full multicomponent diffusion coefficient matrices for silicate melts, an effective binary diffusion model is used to obtain an order-of-magnitude approximation of cooling duration. Si was chosen because, as the most abundant cationic component, its diffusivity should be least affected by competing chemical potential gradients (i.e., the cross terms of the diffusion coefficient matrix) (Liang 2010).

Models are implemented via a one-dimensional, implicit, finite difference code that incorporates temperature-dependent (thus, time-dependent) diffusivity. Several model parameters were fixed or narrowly constrained with pertinent experimental and theoretical data and with measured trinitite glass compositions. The primary adjustable model parameters for fitting measured profile shapes are cooling duration (in seconds); initial diffusivities (D_0), which are constrained between 7×10^{-4} and 2×10^{-6} m^2/s; and activation energies (E_a/R), which are constrained between 18000-31500 K based on experimental Si effective binary diffusion data (Zhang et al. 2010). The exact D_0 and E_a values for each

model were adjusted within these ranges to improve the shape of model profile "shoulders"; however, the Si gradient fit was determined primarily by the cooling duration. Model starting temperatures were constrained at 1800-2200 K by condensation equilibria at high-temperature, circum-atmospheric pressure conditions (Ebel 2006; Yoneda and Grossman 1995) and were adjusted within this temperature range as a secondary fitting parameter. Model ending temperatures were fixed at 900 K, based on the glass transition temperatures calculated through the viscosity modeling discussed in the previous section; model runs with lower ending temperatures showed no detectable changes to profile shape, consistent with essentially complete diffusive closure below 900 K. A cooling function in which T decreases linearly with 1/t was chosen in accord with theoretical cooling patterns for the fireball (Izrael 2002). Model input parameters and notes on the modeling approach are tabulated in Supplemental Materials 4.

All six Si profiles are well fit by models with total cooling durations of 3-6 s from peak temperatures of 2050 ± 50 K. These estimates align with the theoretical calculations of fireball temperature evolution (Glasstone and Dolan 1977; Izrael 2002; Stewart 1956) and with more recent estimates of melt formation and solidification timescales (Belloni et al. 2011; Cassata et al. 2014; Eby et al. 2015). Both the observation that element diffusion distances are limited to a few 10's of micrometers and the short duration of melt existence as indicated by diffusion modeling suggest that diffusive exchange did not significantly alter or homogenize the different trinitite melt compositions. The short time between melt condensation and melt solidification also supports the earlier conclusion based on viscosity modeling that melt mixing was very limited.

5.3 Oxidation conditions in the fireball

Previous models of fallout formation assumed generally oxidizing conditions within the fireball because it forms in atmosphere (e.g., Adams 1960; Freiling et al. 1965). Raman spectroscopy data from some CaMgFe glasses suggest the presence of reduced forms of carbon (e.g., graphite, CH_2 and CH_3; Fig. 6), which are consistent with high C/O ratios in the fireball, at least transiently, during the condensation of CaMgFe melts. The inference of reducing conditions based on these carbon data aligns with a recent fallout study in which Cassata et al. (2014) found that fissionogenic Xe isotope ratios were more consistent with condensation of Xe parents as atomic or ionic species than as oxide species. Additionally, reduced carbon in aerodynamic debris suggests that reducing conditions inferred from metallic or sulfide spheroids within some amorphous trinitite debris (Bellucci and Simonetti 2012; Eby et al. 2010; Eby et al. 2015) were widespread.

High temperatures within the fireball, as well as sub-atmospheric pressures behind the migrating shockwave (Glasstone and Dolan 1977), likely contributed to the development of reducing conditions within the fireball. Data of this study do not provide constraints on the duration or spatial distribution of reducing conditions in the fireball; however, it seems probable that, generally, the fireball would have progressed from more reducing to more oxidizing conditions through time. If the transition occurred during condensation of CaMgFe melts, then different domains within CaMgFe glass would record different oxidation conditions within the fireball.

5.4 Relative chronology of fallout assembly

Both textures and compositional trends provide clues to the relative formation and assembly chronology of mm-scale trinitite beads. Generally, beads are CaMgFe glass with inclusions of other glass and mineral phases. Some of these inclusion phases likely served as condensation nuclei, though many may also have been free particles that collided with and were captured by already-condensed melts. A nucleus-condensate relation implies that some of the inclusion materials were present within the cloud prior to or during condensation of the CaMgFe melts. The observed host-inclusion relations require that inclusion phases were, at the very least, present in the cloud while much of the CaMgFe phase was still molten. Compositional variations within the CaMgFe glass suggest either an extended period of condensation or multiple condensation episodes over time (and/or space). Consequently, the formation of debris constituents – melt droplets, melt-coated ground-derived particles, and uncoated ground-derived particles – was probably diachronous, spanning the time when temperature conditions were appropriate for condensation and continuing until all CaMgFe melts solidified. Furthermore, these condensation and melt conditions may have existed and persisted for different periods of time in different parts of the fireball.

Assembly of smaller particles into macroscopic fallout beads likely occurred as the number density of particles within the fireball increased by a combination of condensation and turbulent ground material entrainment. The presence of multiple, disseminated inclusions within a single larger piece of aerodynamic debris indicates collision and agglomeration of many particles to form the mm-scale, “smooth” beads. The compound structure of bead #11 (Fig. 2, 3), in which an amorphous piece of glass is adhered to and partially wraps around a well-formed smooth bead, provides evidence that once assembled, macroscopic debris continued to experience collision and agglomeration. Textural features of the “lumpy”, irregular beads are consistent with their late formation by collision of already-assembled but still-molten smooth beads with lechatelierite blebs and mineral aggregates. The glass rinds of irregular beads display the same assemblage of constituents and host-inclusion textures as the smooth

beads. The existence of mineral aggregates within the fireball, rather than individual particles, requires a grain-adhering mechanism, which was apparently provided by solidification of the partial melts that are currently observed as Ca-rich glass along grain boundaries (Fig. 3: #6,7,8,14). Additionally, the contacts between mineral aggregates and glassy rinds are lined with vesicles, indicating rapid quenching and volatile exsolution as melts collided with the relatively cool mineral aggregates (Fig. 3: #6,7,8).

Compositional variations within the CaMgFe glasses provide a relative condensation chronology, when interpreted in the context of element volatility. The relative volatility of a given glass composition can be assessed by determining its position in volatility space (Fig. 12) as defined by the abundances of refractory (Al, Ca, Ti), transitional (Mg, Fe, Si), and volatile (Na, K) major elements. Al-Ca-rich, Si-poor domains of CaMgFe glass (beads #8 and #14 in Figs. 3 and 4B) are the most refractory CaMgFe glass compositions, plotting closest to the refractory apex of the major-element volatility diagram (Fig. 12), and they thus are inferred to be the earliest-formed debris constituents. The precursor melts of these refractory glasses would have condensed from the fireball before melt compositions dominated by lower-condensation-temperature transitional and volatile elements. Within the set of samples investigated for this study, refractory CaMgFe glasses do not contain inclusions of other phases, consistent with the inference that they formed early during fireball development when inclusion phases were either not yet present or not yet abundant in the fireball. The early, refractory melts appear to be the compositional endmember of a nearly linear trend (in volatility space) of correlated decreasing refractory-element and increasing transitional- and volatile-element abundance (Fig. 12). This trend suggests that the major-element composition of CaMgFe glasses can be used as a proxy for relative condensation time.

5.5 Updated model for the formation of glassy fallout debris

Major-element composition and textural data suggest the following chronology of trinitite debris formation. Upon detonation, materials from the ground, tower, and device were fragmented and vaporized by intense radiative heating, forming a compositionally heterogeneous plasma. The expanding shockwave displaced atmosphere within a rolling, low-pressure, low-f_{O2} region in its wake in which droplets of highly refractory, Ca-Al-rich melts condensed (Fig 13, time 1). The intersection of the shockwave and the ground surface entrained loose sand grains into the developing fireball, where many were heated to the point of melting, and some to the point of evaporation. On the ground, radiant heating induced localized partial melting of sediment. Strong turbulence developed within the fireball as air rushed back in following atmospheric displacement by the passing shockwave. Partially to fully molten sediment grains present in the cloud served as nuclei for the condensation of progressively more

oxidized and silica-rich melts from the fireball plasma. Collisions and agglomeration of condensed melt droplets and condensation-coated grains produced smooth, spheroidal melt beads containing refractory condensates, individual quartz grains, silica melt blebs, and/or feldspar melt blebs (Fig. 13, time 2). Turbulence within the cloud produced strong temperature gradients, and many agglomerated beads quenched rapidly to glass. Turbulence at the ground surface continued to scour and deliver solid grains and melt-adhered grain aggregates into the cloud, where some collided with the remaining molten condensate beads (Fig. 13, time 3). The force of the collision with mineral aggregates disrupted condensed melt beads, spreading melt over the surfaces of grain aggregates, where it quenched rapidly to a glassy rind. Fallout occurred shortly thereafter. The entirety of debris formation, from vaporization to fallout, likely took on the order of 10 seconds or less.

5.5 Trinitite analogues and synthetic surrogates

Natural glasses commonly cited as analogues for trinitite include fulgurites and tektites (Eby et al., 2010; Bunch et al., 2012; Eby et al., 2015) because of their high-energy, catastrophic origins. Several authors also point to fundamentally magmatic-type processes – partial melting, melt mixing, melt immiscibility – to explain the compositional variation in trinitite (Bellucci et al. 2014; Eby et al. 2015; Koemen et al. 2013; Lewis et al. 2015; Wallace et al. 2013). It is useful therefore to compare trinitite glass and natural glass compositions (Fig. 12) in order to understand the magnitude and direction of elemental fractionation produced by natural processes versus those produced by the Trinity explosion.

Terrestrial volcanic glasses overlap compositionally with the transitional- and volatile-element-enriched CaMgFe glass (Fig. 12), but even considering basaltic and rhyolitic populations together, magmatic rocks do not approach the compositional range of CaMgFe glasses. The trends of volcanic rocks in volatility space do nonetheless provide a sense of the type and amount of compositional variability that can be produced by magmatic processes alone. Both basaltic and rhyolitic trends are subhorizontal on the volatility space diagram, indicating i) greater fractionation of refractory and transitional elements than volatile elements, and ii) weak or no coupling between magmatic processes that fractionate volatile elements and magmatic processes that fractionate refractory and transitional elements. The second point particularly distinguishes magmatic processes from condensation, in which the relative abundances of refractory, transitional, and volatile elements should all covary. For comparison, trinitite CaMgFe glasses demonstrate the expected condensation covariation: decreasing refractory element abundance is correlated with increasing transitional and volatile element abundances, producing a diagonal trend in volatility space.

Fulgurite glass compositions overlap with trinitite silica-rich glasses, trinitite alkali-rich glasses, and with the volatile to transitional trinitite CaMgFe glasses (Fig. 12). The ubiquity of lechatelierite and other fulgurite textures indicate that the spatially focused energetic input of lightening results in selective melting of some minerals and incongruent partial melting or partial evaporation of others (Martin Crespo et al. 2009; Pasek et al. 2012). Thus, fulgurites appear to form by the strongly disequilibrium melting and evaporation processes that have been proposed in some models of trinitite formation (e.g., Bellucci et al. 2012; Bellucci et al. 2014; Eby et al. 2015). Even so, within the limits of the sparse data available, fulgurite glasses do not span the compositional range or reach the compositional extremes of the trinitite CaMgFe glasses (Fig. 12). Several fulgurites show a progression from more refractory-enriched interior glasses to more volatile-enriched exterior glasses, suggesting that evaporated constituents condense to melt over very short length scales (Joseph 2012) and, thus that fulgurites are essentially closed systems. In Figure 12, the most refractory fulgurite glasses define a trend that approximately parallels the main CaMgFe glass trend but is shifted toward higher volatile-element content, which is consistent with formation of the fulgurite glasses by partial evaporation and proximal condensation without significant loss of volatiles. We conclude that the spatially heterogeneous heat distribution resulting from channelized lightning-strike electrical conduction does not produce thermal conditions suitable for pervasive or sustained evaporation-condensation.

Compositions of well-preserved tektites and microtektites (glassy impactites) are dominated by transitional (Si, Mg, Fe) elements and are characteristically low in volatile elements (Glass and Simonson 2013; Simonson and Glass 2004). Most tektites are regarded as far-flung impact melts (Glass and Simonson 2013). Some workers propose that microtekites, in contrast, formed by condensation from a plume of vaporized material ejected into or beyond Earth's atmosphere by an impactor (Elkins Tanton et al. 2002; Glass and Simonson, 2013; Heide et al. 2001; von Engelhardt et al. 1987; von Engelhardt et al. 2005). Tektite and microtektite compositions define linear trends that overlap with part of the CaMgFe glass trend (Fig. 12), but they do not show the compositional range or refractory extremes of the CaMgFe glasses. The magnitude of compositional variability in tektites is similar to that found in basaltic to rhyolitic rocks (e.g., Belza et al. 2015; Montanari et al. 1983), consistent with the interpretation that tektites formed by melting of a wide range of target rock lithologies. Microtektites extend toward more volatile and more refractory compositions than tektites (Fig. 12), consistent with loss of volatile elements during vaporization. The limited microtektite compositional range could reflect vaporization of partially melted target rock, rather than direct vaporization of the solid target rock itself (e.g., Johnson and Melosh 2014). Alternatively, more refractory vapor-plume condensates are not present in

microtektites (i.e., glass-dominated impactites) but instead were incorporated into other types of impactites, such as metallic or crystalline spherules (Ebel and Grossman 2005; Glass et al. 2004; Kyte and Bostwick 1995; Smit et al. 1992).

In summary, although fulgurite and microtektite glasses may both form, at least in part, by condensation, they are imperfect analogues for trinitite formation. If anything, fulgurite and microtektite formation regimes bracket the scale and energetic conditions of trinitite formation, producing compositional trends that are in some ways similar to but in other ways quite different from those documented in trinitite. Fulgurites appear to represent a smaller-scale, spatially heterogenous thermal regime marked by strongly disequilibrium partial melting and localized partial evaporation. Microtektites represent a very large-scale, high-energy formation regime with significant physical fractionation of vaporized constituents, such that most volatile elements and possibly many refractory elements were partitioned into different impactite reservoirs that are not represented in glassy microtektite populations.

Interestingly, the major-element compositions of endmember refractory CaMgFe glasses are most comparable to materials formed by condensation from the early solar nebula – specifically, calcium-aluminum-rich inclusions (CAIs) (Fig. 12). CAIs formed by direct, equilibrium vapor-to-solid condensation from a vapor with a very different composition from that of the inferred Trinity fireball plasma (e.g., Krot et al. 2009; Yoneda and Grossman 1995). CaMgFe melts more likely formed by kinetic (Rayleigh) condensation in response to very rapid cooling. Nonetheless, the compositional similarity between CAIs and refractory trinitite provides further evidence that volatility-controlled condensation was the dominant process in CaMgFe melt and glass formation.

Finally, several recent studies have explored the feasibility of producing nuclear-explosion surrogate materials in the lab for calibration and verification of nuclear forensic analytical techniques (e.g., Carney et al. 2013; Liezers et al. 2015; Molgaard et al. 2015). The work of Carney et al. (2013) focused on the creation of glasses with a homogeneous distribution of radioactive elements by sol-gel-type synthesis and furnace heating, whereas the experiments of Molgaard et al. (2015) and Liezers et al. (2015) were aimed at producing texturally heterogeneous glasses similar in appearance to trinitite through furnace or laser heating, respectively. The resulting glass surrogate compositions seem to reflect predominantly melting processes. For instance, Liezers et al. (2015) report elemental fractionation patterns within product glasses – enrichment in high field strength elements (Hf, Nb, Ta Zr), rare earth elements, and large ion lithophile elements (K, Ba, Sr, Pb); depletion in platinum group elements (Pt, Au) and transition metals (Fe, Mn, Cr) – that are more readily explained by partitioning of

incompatible trace elements into a partial melt (e.g., White 2015) than by differential evaporation or condensation of elements. Thus, while surrogate glasses produced so far are useful physical representatives of trinitite and other glassy debris, it is unlikely that they accurately represent the chemical (and isotopic) characteristics of condensation-formed aerodynamic debris.

5.6 Radioisotopic signatures in fallout

The trinitite data presented in this study and the model proposed on the basis of this data have several implications for the incorporation and preservation of radioisotopic signatures within fallout debris. The first and most fundamental is that condensation is the main mechanism for incorporating radioisotopes into glassy fallout. Although most early studies envisioned condensates as consisting primarily of refractory device-derived species, this study suggests that a significant portion of at least aerodynamic trinitite is made up of evaporated and condensed material, and that device-derived radioisotopes are present only as trace species within these bulk condensates. Thus, the condensation chronology recorded in major-element composition trends is also the condensation chronology of trace, device-derived isotopes. This chronology can be a powerful tool for locating compositional regions within debris that preserve radioisotopic signatures of interest.

A second implication is that device-derived isotopic constituents are likely to become fractionated as a result of compositional controls on condensation order. This idea is not new (Freiling 1961; Freiling et al. 1965; Izrael 2002), but our trinitite data provide new constraints on how it occurs. The data support at least two, possibly three, distinct periods of condensation – one very early during the explosion and another, more extended period during expansion and maturation of the fireball. While the large range in CaMgFe glass compositions attests to the protracted condensation, the average elemental enrichments and depletions (Fig. 8) suggest that, volumetrically, aerodynamic debris contains predominantly transitional-volatility condensates. Although some highly refractory glass compositions occur within the debris, the CaMgFe glasses are, on average, neither enriched nor depleted in Al (the most refractory major element), enriched in somewhat less refractory elements (Ca and Fe), neither enriched nor depleted in transitional elements (Si and Mg), and depleted in volatile elements (K and Na). The apparent bias toward more transitional-volatility condensates may indicate that the greatest total quantity of melt condensed during the transitional volatility conditions. If this is the case, then isotopic data collected through bulk analysis of aerodynamic trinitite, and perhaps other glassy fallout debris, will reflect loss of the most refractory fireball constituents, including both refractory actinides and their early-formed, refractory fission products.

A third implication is that liquid-phase interactions do not substantially alter primary compositional heterogeneities arising from spatially or temporally disparate condensation. Thus, agglomerated pieces of aerodynamic debris, and even possibly some amorphous ground-splatter debris that includes melts rained out from the fireball, will retain their primary condensation-determined radioisotopic compositions. Consequently, single pieces of debris can retain diverse records of the compositional environments within the developing fireball. The breadth of such records can only be determined by compositional analyses at the scale of the compositional heterogeneities – i.e., at the microscale.

6. Conclusions

1. Much of the glass in fallout from the Trinity nuclear test formed by volatility-controlled condensation from a compositionally heterogeneous plasma.

2. Co-condensation of ground-derived and device-derived constituents was the mechanism of radioisotope incorporation into trinitite. Melt mixing and diffusion were inefficient mechanisms for introducing or homogenizing trace, device-derived elements within trinitite melts.

3. An updated model for the formation of macroscopic fallout includes evaporation and condensation of bulk, ground-derived materials and device-derived isotopic constituents, agglomeration of condensates and entrained ground materials, and rapid quenching, all within ≤10 seconds of device detonation.

4. Microscale compositional variability observed within aerodynamic trinitite beads is representative of primary compositional variability within the nuclear fireball. Liquid- and solid-phase interactions did not significantly alter primary condensate, melt, or solid compositions.

5. Trends in the major-element composition of CaMgFe glass arise from differences in element volatility, and thus define a chronology for CaMgFe melt condensation.

6.Neither fulgurites nor microtektites are comprehensive chemical or, by inference, formation-process matches for the main CaMgFe trinitite glasses. However, the most refractory trinitite glasses closely resemble early solar-system condensates.

Acknowledgments

The authors thank Drs. Warren Oldham and Susan Hanson of Los Alamos National Lab for providing the samples used in this work. Dr. Ryna Marinenko is thanked for help in obtaining analytical glass standards. Many thanks to two helpful anonymous reviewers, and Dr. Mark Ghiorso for his efficient editorial handling. This project was funded through the United States Department of Energy, the G. T.

Seaborg Institute for Actinide Science, and the Strategic Outcomes Office at Los Alamos National Lab. Los Alamos National Laboratory, an affirmative action/equal opportunity employer, is operated by Los Alamos National Security, LLC, for the National Nuclear Security Administration of the U.S. Department of Energy under contract DE-AC52-06NA25396. This document has been approved for unlimited release under LA-UR-15-20991.

Table 1 Estimated bulk compositions for the Trinity test site sediment

Fig. 1 Geology of the Trinity test site. (A) Geologic and topographic map of the test site area. Entire map area is within the White Sands Missile Range. Dashed line indicates the Oscura Mountains drainage divide. Geology from the New Mexico Web Map (https://maps.nmt.edu). (B) Photograph of the Ground Zero obelisk with the Oscura Mountains to the east. Bedrock units are annotated near the righthand side of photo. (C)-(D) Representative photographs of the backfilled arkose to lithic arkose sediments currently present at the test site. Boot tip for scale. (C) Most common substrate type in the vicinity of ground zero. Coarse-grained sediment comprising predominantly quartz and feldspar grains with lesser limestone fragments. Green trinitite glass fragments also visible. (D) Patch of gravel-sized lithic fragments in a silty matrix. Gravel-sized material includes gray limestone with calcrete crusts and pinkish granitoid. (E)-(G) Representative photographs of rocks and sediment at the McDonald Ranch house, where the ground has been less disturbed than at the Trinity Site. Finger or boot tip for scale. (E) Granitoid boulder in the McDonald Ranch house fence wall. (F) Limestone boulder with fossils fallen from the McDonald Ranch house fence wall. (G) Coarse-grained sediment comprising predominantly quartz and feldspar grains with lesser limestone fragments

Fig. 2 Photographs of aerodynamic trinitite debris samples used for this study. (A) Debris samples before cross-sectioning and microanalysis preparation. Note that beads 4 and 5 are not pictured before sample preparation, but are shown in cross-section in B. Bead 6 fragmented prior to being photographed; fragments are shown. Beads 4, 5, 9, 10, 11, and 12 are, or include, “smooth” spheroids. Beads 6, 7, 8, 13, and 14 are “lumpy”, imperfect spheroids. Beads 9 and 11 are composite objects, comprising portions of two or more single spheroids. (B) Trinitite debris prepared for microanalysis, embedded in epoxy mounts along with glass standard reference materials

Fig. 3 Compilation of phase maps (left) and activity maps (right) of aerodynamic trinitite debris. All images are at the same scale, shown by the 2-mm scale bar at left. Legend shows applicable color scales. (A) Smooth spheroidal beads – both whole and fragmentary. (B) Irregular beads containing mineral aggregates. (C) Irregular beads containing lechatelierite. Features are indicated by the following labels: MCMA = melt-cemented mineral aggregate; L = lechatelierite. Arrows indicate most refractory CaMgFe glass domain

Fig. 4 Summary plots of elemental abundances measured by electron microprobe of trinitite glasses, showing absolute abundances of elements and the variability of each element within each bead. Each square symbol represents elemental abundance determined from one EPMA analysis spot; symbols are larger than analytical uncertainties. The total number of analysis spots per bead is indicated. (A) Compositions of alkali-rich glasses, by individual bead and in aggregate. Mg and Ti abundances are below detection for alkali glass measurements and not shown. Compositions of representative feldspars compositions are shown by symbols at far right for reference. Dashed line connecting symbols indicates possible range of element abundance between high and low feldspar end members. Note the similarity between measured glass composition ranges and feldspar compositions ranges. (B) Compositions of CaMgFe glasses, by individual bead and in aggregate. The estimated bulk test-site sediment (Table 1) compositional ranges are shown at far right for comparison. Note that element order is different in A and B, in order to more clearly show the trends in the different glasses. All EPMA data are tabulated in Supplemental Materials Table 1

Fig. 5 (A) Correlation plots for all major and minor elements in CaMgFe glasses. Correlation coefficients are shown in the upper right or left of each plot. (B) Principal component analysis of major elements in CaMgFe glasses

Fig. 6 Laser Raman spectra for five locations in CaMgFe glass. Spectra are offset to more clearly display spectral features, but the vertical scaling is the same for all spectra. Peaks greater than 1250 cm^{-1} that suggest the presence of reduced forms of carbon are annotated. Dashed lines labeled D and G indicate the typical positions of the D and G bands of graphite. See text for discussion

Fig. 7 Trinitite CaMgFe glass (black) and alkali glass (blue) data plotted on a total alkali-silica diagram

Fig. 8 Box-and-whisker plot showing the enrichment and depletion of elements within the CaMgFe glass relative to the average bulk sediment composition (Table 1). All CaMgFe glass compositional data are represented (Appendix 1). Lower and upper edges of the boxes indicate the positions of the first and

third quartile of the data, respectively. Median value shown by the horizontal gray line. Whiskers extend to include 99.3% of the data range relative to the median. Data that fall outside the 99.3% range are shown by gray crosses. Values greater than one indicate enrichment in the element relative to the bulk sediment, whereas values less than one indicate depletion relative to the bulk sediment composition. Relative condensation temperature order based on 50% condensation temperatures from Lodders (2003)

Fig. 9 Temporal development of the nuclear fireball. Red curve is illumination measured for ~20-kT Trinity explosion with calculated estimates of fireball surface temperature indicated (Bainbridge, 1976). Hermes and Strickfaden (2005) calculated an "average fireball temperature" for Trinity of 8430 K, presumably for a time around the second thermal maximum. The blue curve is a schematic representation of pressure variation at a point within the inner fireball based on Glasstone and Dolan (1977). Plot is annotated with elements of fireball development as described in Glasstone and Dolan (1977) and Izrael (2002). The breakaway is the time when the opaque, shock-heated outer surface of the fireball cools and becomes transparent enough to allow radiation from the inner, hotter part of the fireball to escape; it marks the transition from a faster shock-wave driven expansion to a slower radiative-heating driven expansion of the fireball. The inner part of the fireball is presumed to be hotter than the outer surface at all times. Condensation of vaporized ground and device material occurs following the second thermal maximum

Fig. 10 Viscosity as a function of temperature for melt precursors to trinitite alkali-rich (blue) and CaMgFe (pink) melts. Viscosities are calculated based on measured compositions of alkali and CaMgFe glasses using the model of Giordano et al. (2008) as implemented in on-line viscosity calculator available at http://www.eos.ubc.ca/~krussell/VISCOSITY/grdViscosity.html. Green line segment shows experimentally determined viscosity for melted quartz at 1 atmosphere (Ryan and Blevins, 1987) as an indication of the expected viscosity of trinitite silica glasses. Inset shows a histogram of calculated glass transition temperatures (T_g), which provide an estimates of the temperatures at which the different melts solidified

Fig. 11 Si diffusion profiles and model fits (red solid lines). Insets are BSE images of trinitite beads showing the location of the EPMA traverses and plots showing element variations along each EPMA traverse. Arrows indicate the modeled segment(s) of each traverse. Temperature range and cooling

duration in seconds indicated for each profile model fit. (A) 8768-5, traverse 2. (B) 8768-5, traverse 4. (C) 8768-6, fragment B, traverse 1. (D) 8768-12, traverse 3, and (E) 8768-8, traverse 1

Fig. 12 Ternary volatility space diagram for major elements showing the compositional trends of trinitite glasses and other natural materials. The average composition of the upper continental crust is also plotted for reference (black hexagon). Basalt and rhyolite data from PetDB (Lehnert et al 2000). Tektite data from Bentor (1986); Dressler and Reimold (2001); Lee et al. (2004); Son and Koeberl (2005); von Engelhardt et al. (2005); Amare and Koeberl (2006); Koeberl et al. (2007); Lin et al. (2011). Microtektite data from Koeberl et al. (1997); Glass et al. (2004); Folco, et al. (2009); Belza et al. (2015). CAI data from Grossman et al. (2000). Fulgurite data from Bentor (1986); Martin Crespo et al. (2009); Carter et al. (2010); Pasek et al. (2012)

Fig. 13 Model for macroscopic trinitite fallout formation. Temperature (red) and pressure (blue) curves are schematic. Condensation begins at time 1 with highly refractory Ca-Al-rich, Si-poor melts. Convection and turbulence deliver ground material into the cloud and condensation accelerates at time 2. Condensates become progressively more Si- and alkali-rich. Condensation ceases around 3, but macroscopic debris continues to form by agglomeration of still molten droplets, mineral debris, and melt-coated ground nuclei

References

Adams, CE, Farlow, NH, Schell, WR (1960) The compositions, structures and origins of radioactive fall-out particles. Geochim Cosmochim Ac 18:42-56.

Amare, K, Koeberl, C (2006) Variation of chemical composition in Australasian tektites from different localities in Vietnam. Meteorit Planet Sci 41: 107-123.

Atkatz, D, Bragg, C (1995) Determining the yield of the Trinity nuclear device via gamma-ray spectroscopy. Am J Phys 63: 411-413.

Bainbridge, KT (1976) *Trinity*. Los Alamos Scientific Laboratory, Los Alamos, NM.

Belloni, F, Himbert, J, Marzocchi, O, Romanello, V (2011) Investigating incorporation and distribution of radionuclides in trinitite. J Environ Radioactiv 102: 852-862.

Bellucci, JJ, Simonetti, A (2012) Nuclear forensics: searching for nuclear device debris in trinitite-hosted inclusions. J Radioanal Nucl Ch 293: 313-319.

Bellucci, JJ, Simonetti, A, Koeman, EC, Wallace, C, Burns, PC (2014) A detailed geochemical investigation of post-nuclear detonation trinitite glass at high spatial resolution: Delineating anthropogenic vs. natural components. Chem Geol 365:69-86.

Belza, J, Goderis, S, Smit, J, Vanhaecke, F, Baert, K, Terryn, H, Claeys, P (2015) High spatial resolution geohemistry and textural characteristics of 'microtektite' glass spherules in proximal Cretaceous-Paleogene sections: Insights into glass alteration patterns and precursor melt lithologies. Geochim Cosmochim Ac 152: 1-38. doi: 10.1016/j.gca.2014.12.013.

Bentor, YK (1986) A new approach to the problem of tektite genesis. Earth Planet Sc Lett 77:1-13.

Bunch, TE, Hermes, RE, Moore, AMT, Kennett, DJ, Weaver, JC, Wittke, JH, DeCarli, PS, Bischoff, JL, Hillman, GC, Howard, GA, Kimbel, DR, Kletetschka, G, Lipo, CP, Sakai, S, Revay, Z, West, A, Firestone, RB, Kennett, JP (2012) Very high-temperature impact melt products as evidence for cosmic airbursts and impacts 12,900 years ago. P Natl Acad Sci USA 109:E1903-E1912.

Carney, KP, Finck, MR, McGrath, CA, Martin, LR, Lewis, RR (2013) The development of radioactive glass surrogates for fallout debris. J Radioanal Nucl Ch 299: 363-372.

Carter, EA, Hargreaves, MD, Kee, TP, Pasek, MA, Edwards, HGM (2010) A Raman spectroscopic study of a fulgurite. Philos T R Soc A 368:3087-3097.

Cassata, WS, Prussin, SG, Knight, KB, Hutcheon, ID, Isselhardt, BH, Renne, PR (2014) When the dust settles: stable xenon isotope constraints on the formation of nuclear fallout. J Environ Radioactiv 137:88-95.

Dai ZR, Crowhurst JC, Grant CD, et al (2013) Exploring high temperature phenomena related to post-detonation using an electric arc. Journal of Applied Physics 114:204901. doi: 10.1063/1.4829660

Davis, A, Richter, F (2003) Condensation and evaporation of solar system materials. In: Davis, A (ed) Meteorites, Comets and Planets. Elsevier, pp 407-430.

de Niem, D, Kührt, E, Motschmann (2008) Initial condensate composition during asteroid impacts. Icarus 196: 539-551. doi:10.1016/j.icarus.2008.03.012.

Donovan, J (2016) Probe for EPMA User's Guide and Reference. Probe Software, Eugene, Oregon.

Dressler, BO, Reimold, WU (2001) Terrestrial impact melt rocks and glasses. Earth-Science Reviews 56:205-284.

Ebel, DS (2006) Condensation of rocky material in astrophysical environments. In: Lauretta, DS, McSween Jr., HY (eds.) Meteorites and the Early Solar System II. University of Arizona, Tucson, pp 253-277.

Ebel, DS, Grossman, L (2005) Spinel-bearing spherules condensed from the Chicxulub impact-vapor plume. Geology 33: 293-296. doi: 10.1130/G21136.1.

Eby, GN, Charnley, N, Pirrie, D, Hermes, R, Smoliga, J, Rollinson, G (2015) Trinitite redux: Mineralogy and petrology. Am Mineral 100:427-441.

Eby, N, Hermes, R, Charnley, N, Smoliga, JA (2010) Trinitite—the atomic rock. Geology Today 26:180-185.

Elkins Tanton, LT, Kelly, DC, Bico, J, Bush, JWM (2002) Microtekites as vapor condensates, and a possible new strewn field at 5 Ma. Lunar and Planetary Science Conference 33:1622.

Eppich, G, Knight, K, Jacomb-Hood, T, Spriggs, G, Hutcheon, I (2014) Constraints on fallout melt glass formation from a near-surface nuclear test. J Radioanal Nucl Ch 302:593-609.

Fahey, AJ, Zeissler, CJ, Newbury, DE, Davis, J, Lindstrom, RM (2010) Postdetonation nuclear debris for attribution. P Natl Acad Sci 107:20207-20212.

Folco, L, D'Orazio, M, Tiepolo, M, Tonarini, S, Ottolini, L, Perchiazzi, N, Rochette, R, Glass, BP (2009) Transantarctic Mountain microtektites: Geochemical affinity with Australasian microtektites. Geochim Cosmochim Ac 73:3694-3722.

Freiling, EC (1961) Radionuclide fractionation in bomb debris. Science 133:1991-1998.

Freiling, EC, Crocker, GR, Adams, CE (1965) Nuclear debris formation. In: Klement, AW (ed) Radioactive fallout from nuclear weapons tests. US Atomic Energy Commission, Germantown, Maryland, pp 1-41.

Giordano, D, Russell, JK, Dingwell, DB (2008) Viscosity of magmatic liquids: A model. Earth Planet Sc Lett 271:123-134.

Glass, BP, Huber, H, Koeberl, C (2004) Geochemistry of Cenozoic microtektites and clinopyroxene-bearing spherules. Geochim Cosmochim Ac 68:3971-4006.

Glass, BP, Simonson, BM (2013) Distal impact ejecta layers. Springer.

Glasstone, S, Dolan, PJ (1977) The effects of nuclear weapons. US Government Printing Office.

Grossman, L, Ebel, DS, Simon, SB, Davis, AM, Richter, FM, Parsad, NM (2000) Major element chemical and isotopic compositions of refractory inclusions in C3 chondrites: the separate roles of condensation and evaporation. Geochim Cosmochim Ac 64:2879-2894.

Hanson, SK, Pollington, AD, Waidmann, CR, Kinman, WS, Wende, AM, Miller, JL, Berger, JA, Oldham, WJ, Selby, HD (2016) Measurement of extinct fission products in nuclear bomb debris: Determination of the yield of the Trinity nuclear test 70 y later. doi: 10.1073/pnas.1602792113.

Heide, K, Heide, G, Kloess, G (2001) Glass chemistry of tektites. Planet Space Sci 49:839-844.

Hermes, RE, Strickfaden, WB (2005) A new look at trinitite. Nuclear Weapons Journal 2005: 2-7.

Huppert, HE, Stephen, R, Sparks, J, Turner, JS (1984) Some effects of viscosity on the dynamics of replenished magma chambers. J Geophys Res-Sol Ea 89:6857-6877.

Izrael, YA (2002) Radioactive fallout after nuclear explosions and accidents. Elsevier, New York.

Johnson, BC, Melosh, HJ (2012) Formation of spherules in impact produced vapor plumes. Icarus 217:416-430.

Johnson, BC, Melosh, HJ (2014) Formation of melt droplets, melt fragments, and accretionary impact lapilli during a hypervelocity impact. Icarus 228:347-363.

Joseph, ML (2012) A geochemical analysis of fulgurites: from the innner glass to the outer crust. Dissertation, University of South Florida.

Kathmann, SM, Schenter, GK, Garrett, BC (2005) Ion-Induced Nucleation: The Importance of Chemistry. Phys Rev Lett 94: 116104.

Knight, KB, Kita, NT, Mendybaev, RA, Richter, FM, Davis, AM, Valley, JW (2009) Silicon isotopic fractionation of CAI-like vacuum evaporation residues. Geochim Cosmochim Ac 73:6390-6401.

Koeberl, C, Bottomley, R, Glass, BP, Storzer, D (1997) Geochemistry and age of Ivory Coast tektites and microtektites. Geochim Cosmochim Ac 61:1745-1772.

Koeberl, C, Brandstätter, F, Glass, BP, Hecht, L, Mader, D, Reimold, WU (2007) Uppermost impact fallback layer in the Bosumtwi crater (Ghana): Mineralogy, geochemistry, and comparison with Ivory Coast tektites. Metorit Planet Sci 42:709-729.

Koeman, EC, Simonetti, A, Chen, W, Burns, PC (2013) Oxygen isotope composition of trinitite postdetonation materials. Anal Chem 85:11913-11919.

Kottlowski, FE (1953) Geology and ore deposits of a part of the Hansonburg Mining District Socorro County. New Mexico Instititute of Mining and Technology, State Bureau of Mines and Mineral Resources Circular 23.

Koyaguchi, T (1989) Chemical gradient at diffusive interfaces in magma chambers. Contrib Mineral Petr 103:143-152.

Krot, AN, Amelin, Y, Bland, P, Ciesla, FJ, Connelly, J, Davis, AM, Huss, GR, Hutcheon, ID, Makide, K, Nagashima, K, Nyquist, LE, Russell, SS, Scott, ERD, Thrane, K, Yurimoto, H, Yin, QZ (2009) Origin and chronology of chondritic components: A review. Geochim Cosmochim Ac 73:4963-4997.

Kyte, FT, Bostwick, JA (1995) Magnesioferrite spinel in Cretaceous/Tertiary boundary sediments of the Pacific basin: Remnants of hot, early ejecta from the Chicxulub impact?. Earth Planet Sc Lett 132: 113-127.

Lee, YT, Chen, JC, Ho, KS, Juang, WS (2004) Geochemical studies of tektites from East Asia. Geochem J 38:1-17.

Lehnert, K, Su, Y, Langmuir, CH, Sarbas, B, Nohl, U (2000) A global geochemical database structure for rocks. Geochem Geophys Geosy 1:1012. doi: 10.1029/1999GC000026

Lewis, LA, Knight, KB, Matzel, JE, Prussin, SG, Zimmer, MM, Kinman, WS, Ryerson, FJ, Hutcheon, ID (2015) Spatially-resolved analyses of aerodynamic fallout from a uranium-fueled nuclear test. J Environ Radioactiv 148:183-195.

Liang, Y (2010) Multicomponent diffusion in molten silicates: theory, experiments, and geological applications. Rev Mineral Geochem 72:409-446.

Liezers, M, Fahey, A, Carman, A, Eiden, G (2015) The formation of trinitite-like surrogate nuclear explosion debris (SNED) and extreme thermal fractionation of SRM-612 glass induced by high power CW CO2 laser irradiation. J Radioanal Nucl Ch 304:705-715.

Lin, S, Guan, YB, Hsu, WB (2011) Geochemistry and origin of tektites from Guilin of Guangxi, Guangdong and Hainan. Sci China Ser D 54:349-358.

Lineweaver, Jm (1963) Oxygen outgassing caused by electron bombardment of glass. J Appl Phys 34, 1786-1791.

Lodders, K (2003) Solar system abundances and condensation temperatures of the elements. Astrophys J 591:1220-1247.

Martin Crespo, T, Lozano Fernandez, RG, Gonzalez Laguna, R (2009) The fulgurite of Torre de Moncorvo (Portugal): Description and analysis of the glass. Eur J Mineral 21:783-794.

Mayer, K, Wallenius, M, Varga, Z (2013) Nuclear forensic science: Correlating measurable material parameters to the hisory of nuclear material. Chem Rev 113:884-900.

Melosh, HJ, Vickery, AM (1991) Melt droplet formation in energetic impact events. Nature 350:494-497.

Miller, C (1960) A Theory of Formation of Fallout from Land-surface Nuclear Detonations and Decay of the Fission Products. Research and Development Technical Report, U.S. Naval Radiological Defense Laboratory, San Francisco, California.

Molgaard, J, Auxier, J, Giminaro, A, Oldham, CJ, Cook, M, Young, S, Hall, H (2015) Development of synthetic nuclear melt glass for forensic analysis. J Radioanal Nucl Ch 304:1293-1301.

Montanari, A, Hay, RL, Alvarez, W (1983) Spheroids at the Cretaceous-Tertiary boundary are altered impact droplets of basaltic composition. Geology 11: 668-671.

Montel, J.-P. and Vielzeuf, D (1997) Partial melting of metagreywackes, Part II. Composition of minerals and melts. Contrib Mineral Petr 128:176-196.

Morfill, GE, Ivlev, AV (2009) Complex plasmas: An interdisciplinary research field. Rev Mod Phys 81:1353-1404.

Morgan, GB, London, D (1996) Optimizing the electron microprobe of hydrous alkali aluminosilicate glasses. Am Mineral 81: 1176-1185.

Mysen, B, Richet, P (2005) Silicate glasses and melts: properties and structure. Elsevier.

Neal, JT, Smith, RE, Jones, BF (1983) Pleistocene Lake Trinity, an evaporite basin in the northern Jornada del Muerto, New Mexico. In: Chapin, CE, Callender, JF (eds) New Mexico Geological Society 34th Annual Field Conference Guidebook. New Mexico Geological Society, pp 285-290.

Parekh, PP, Semkow, TM, Torres, MA, Haines, DK, Cooper, JM, Rosenberg, PM, Kitto, ME (2006) Radioactivity in trinitite six decades later. J Environ Radioactiv 85:103-120.

Pasek, M, Block, K, Pasek, V (2012) Fulgurite morphology: a classification scheme and clues to formation. Contrib Mineral Petr 164:477-492.

Pittauerová, D, Kolb, WM, Rosenstiel, JC, Fischer, HW (2010) Radioactivity in Trinitite-a review and new measurements. Proceedings of Third European IRPA Congress, Helsinki, Finland, pp 14-16.

Reines, F, Penney, WG, Rarita, W, Swinehart, D (1945) July 16th nuclear explosion: Permanent earth displacement. Los Alamos National Laboratory Report LA-365.

Richter, FM, Davis, AM, Ebel, DS, Hashimoto, A (2002) Elemental and isotopic fractionation of Type B calcium-, aluminum-rich inclusions: experiments, theoretical considerations, and constraints on their thermal evolution. Geochim Cosmochim Ac 66:521-540.

Richter, FM, Janney, PE, Mendybaev, RA, Davis, AM, Wadhwa, M (2007) Elemental and isotopic fractionation of Type B CAI-like liquids by evaporation. Geochim Cosmochim Ac 71:5544-5564.

Ryan, MP, Blevins, JYK (1987) The viscosity of synthetic and natural silicate melts and glasses at high temperatures and 1 bar (10^5 Pascals) pressure and at higher pressures. *USGS Bull* 1764.

Schlauf, D, Siemon, K, Weber, R, Esterlund, RA, Molzahn, D, Patzelt, P (1997) Trinitite redux: Comment on “Determining the yield of the Trinity nuclear device via gamma-ray spectroscopy,” by David Atkatz and Christopher Bragg [Am. J. Phys. 63 (5), 411–413 (1995)]. Am J Phys 65:1110-1112.

Sharp, N, McDonough, W, Ticknor, B, Ash, R, Piccoli, P, Borg, D (2014) Rapid analysis of trinitite with nuclear forensic applications for post-detonation material analyses. J Radioanal Nucl Ch 302:57-67.

Simonson, BM, Glass, BP (2004) Spherule layers—records of ancient impacts. Annu Rev Earth Pl Sc 32:329-361.

Smit, J, Alvarez, W, Montanari, A, Swinburne, N, van Kempen, TM, Klaver, GT (1992) ‘Tektites’ and microkrystites at the Cretaceous Tertiary boundary – Two strewn fields, one crater? Proceedings of Lunar and Planteary Science Conference 22: 87-100.

Son, TH, Koeberl, C (2005) Chemical variation within fragments of Australasian tektites. Meteorit Planet Sci 40:805-815.

Stewart, K (1956) The condensation of a vapour to an assembly of droplets or particles. T Faraday Soc 52:161-173.

Thompson, AB (1982) Dehydration melting of pelitic rocks and the generation of H_2O-undersaturated granitic liquids. Am J Sci 282:1567-1595.

Vielzeuf, D, Holloway, JR (1988) Experimental determination of the fluid-absent melting relations in pelitic systems: consequences for crustal differentiation. Contrib Mineral Petr 98:257-276.

Vishnyakov, VI, Kiro, SA, Ennan, AA (2011) Heterogeneous ion-induced nucleation in thermal dusty plasmas. J Phys D Appl Phys 44:215201.

von Engelhardt, W, Berthold, C, Wenzel, T, Dehner, T (2005) Chemistry, small-scale inhomogeneity, and formation of moldavites as condensates from sands vaporized by the Ries impact. Geochim Cosmochim Ac 69:5611-5626.

von Engelhardt, WV, Luft, E, Arndt, J, Schock, H, Weiskirchner, W (1987) Origin of moldavites. Geochim Cosmochim Ac 51:1425-1443.

Wallace, C, Bellucci, JJ, Simonetti, A, Hainley, T, Koeman, EC, Burns, PC (2013) A multi-method approach for determination of radionuclide distribution in trinitite. J Radioanal Nucl Ch 298:993-1003.

Weber, RH (1964) Geology of the Carrizozo quadrangle, New Mexico. In: Ash, SRD (ed) New Mexico Geological Society 15th Annual Fall Field Conference Guidebook. New Mexico Geological Society, pp 100-109.

Winter, JD (2014). Principles of igneous and metamorphic petrology. Prentice Hall, New York.

Yoneda, S, Grossman, L (1995) Condensation of $CaOMgOAl_2O_3SiO_2$ liquids from cosmic gases. Geochim Cosmochim Ac 59:3413-3444.

Zhang, Y, Ni, H, Chen, Y (2010) Diffusion Data in Silicate Melts. Rev Mineral Geochem 72:311-408.

Figure 1

Click here to download Figure Bonamicietal_Fig1.tif

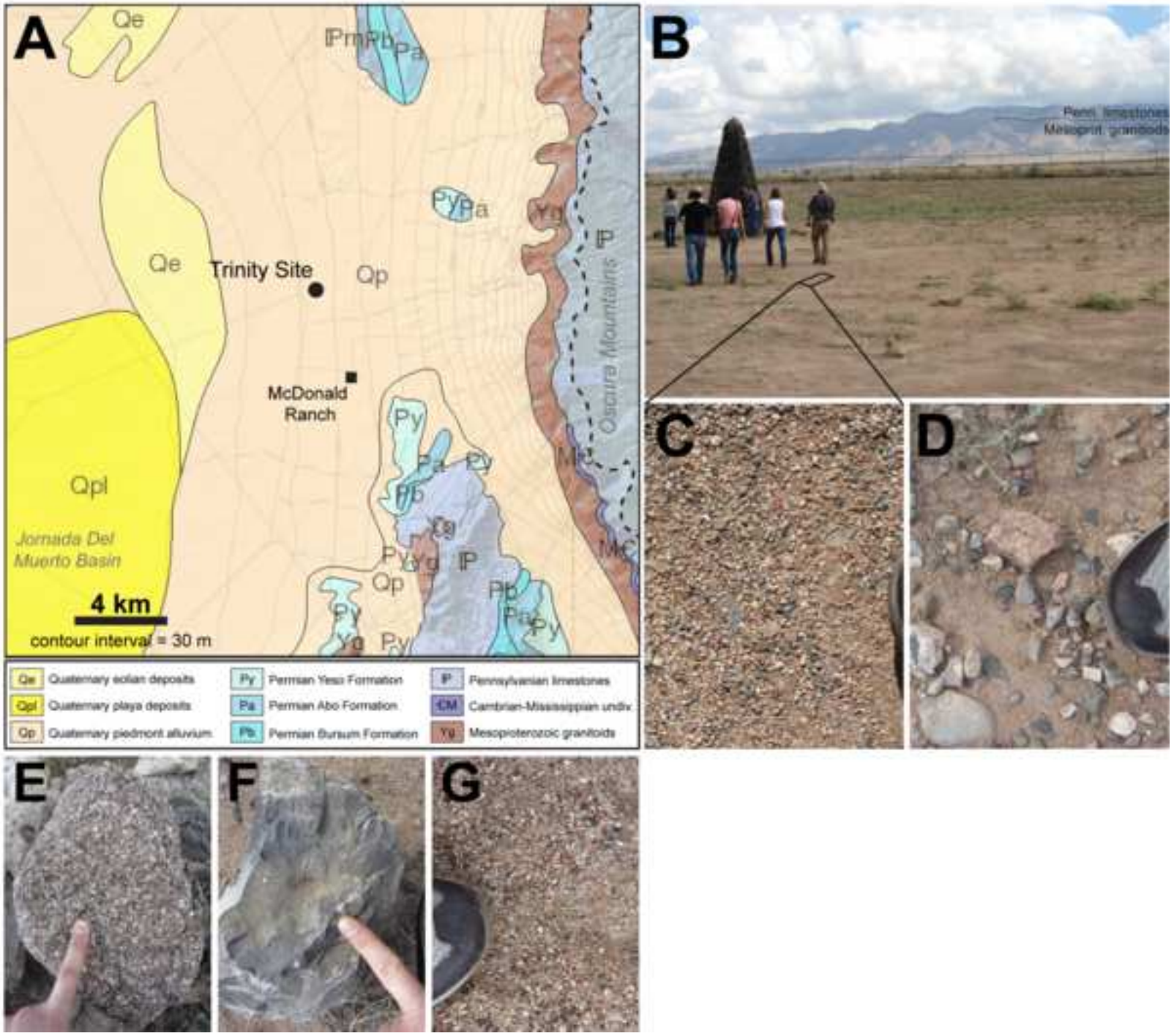

Figure 2

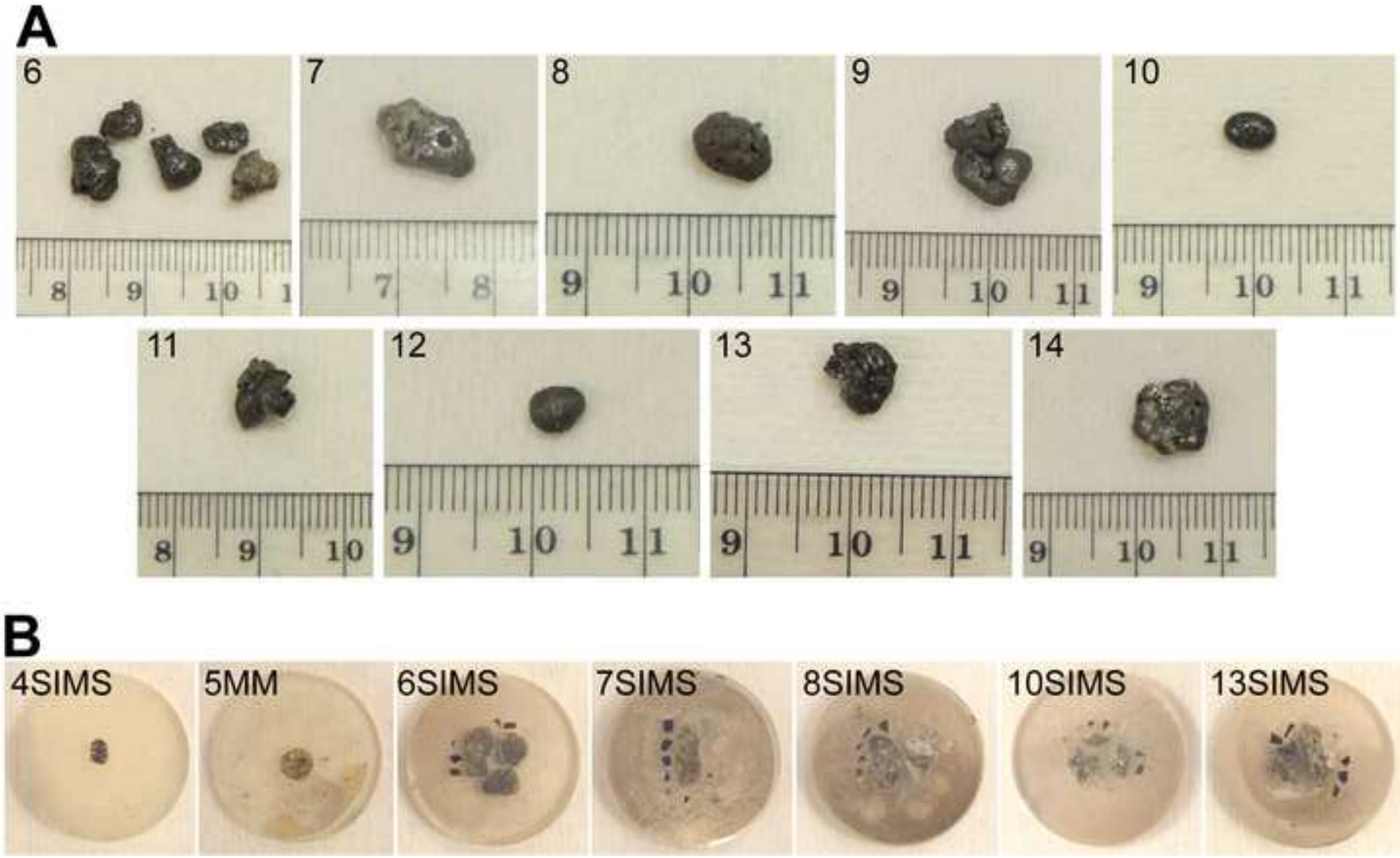

Figure 3

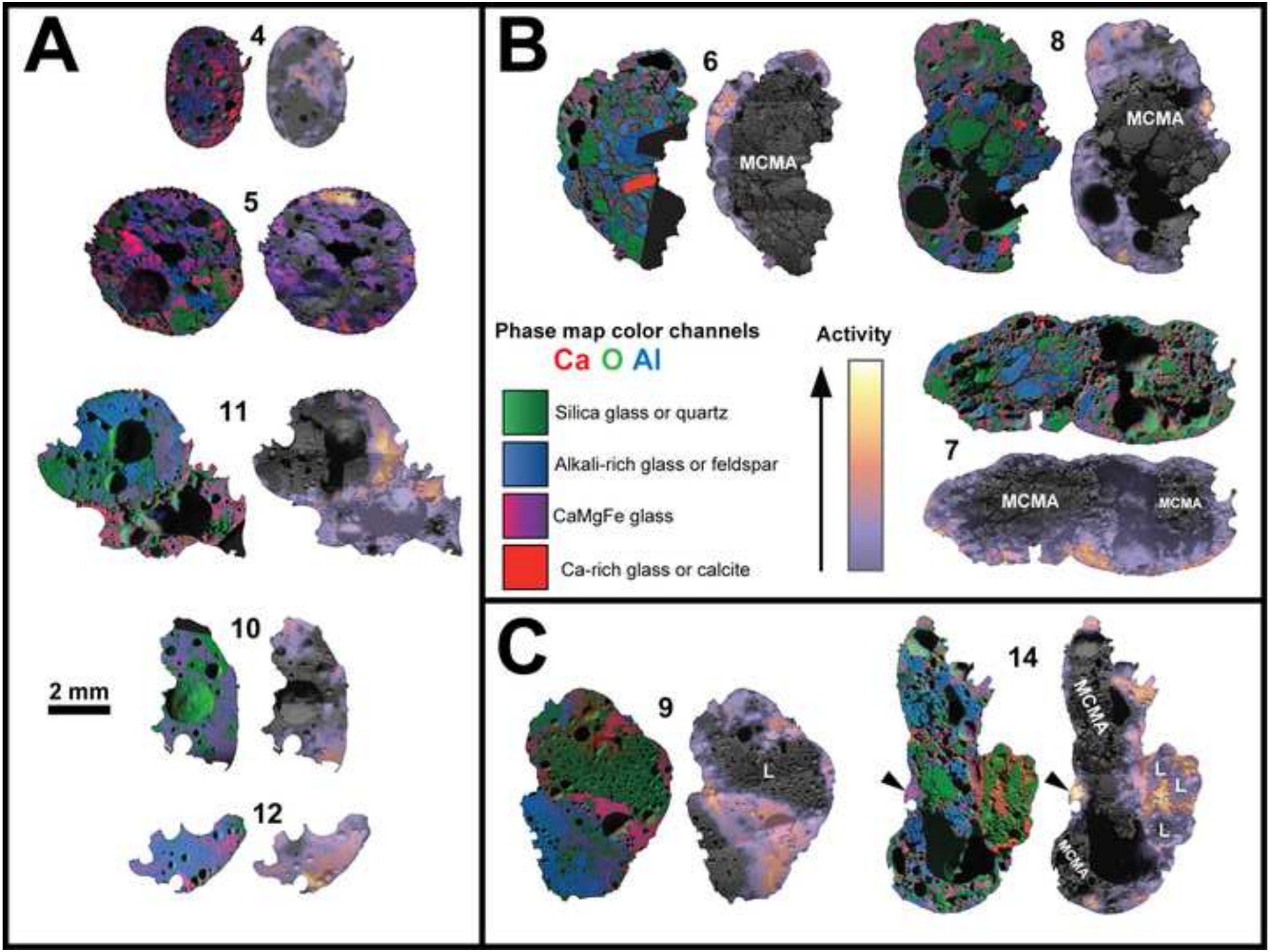

Figure 4

Click here to download Figure Bonamicietal_Fig4.eps

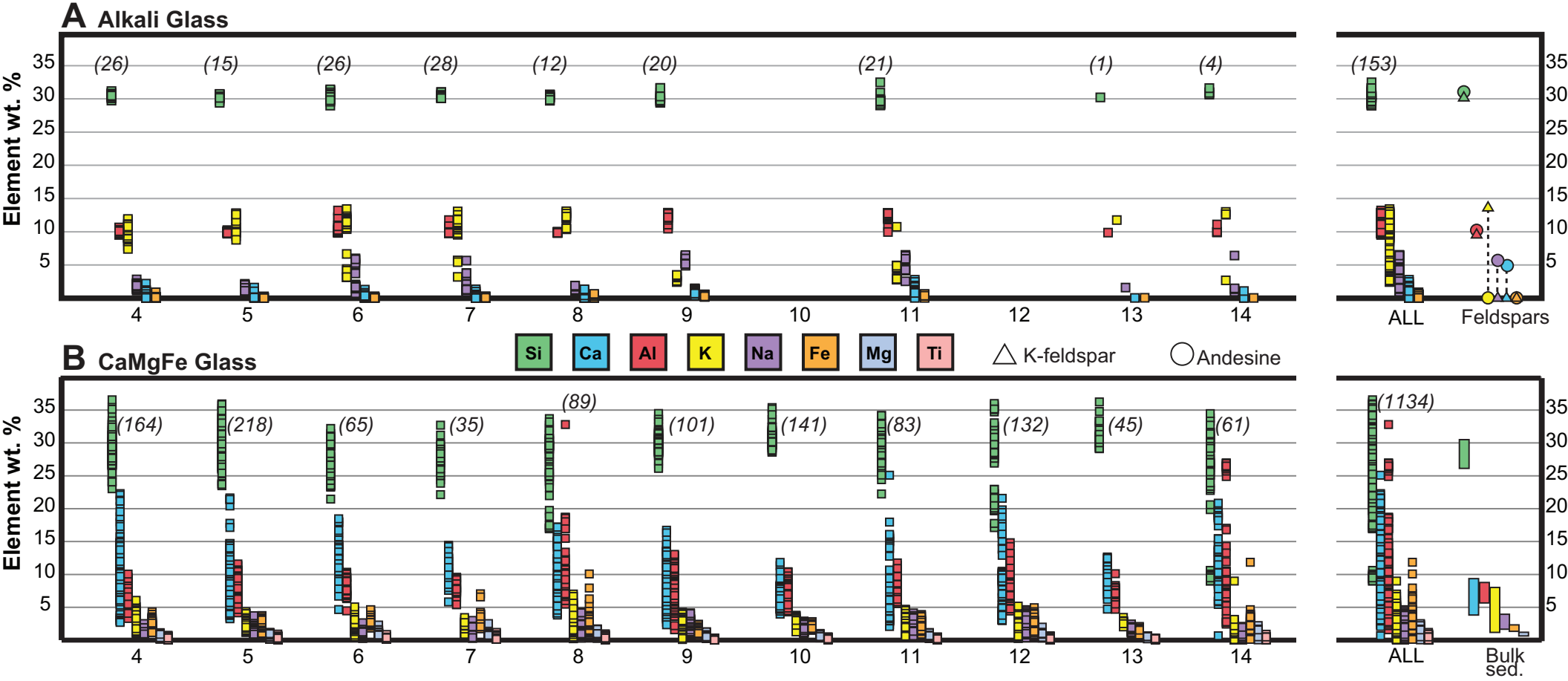

Figure 5

Click here to download Figure Bonamicietal_Fig5.eps

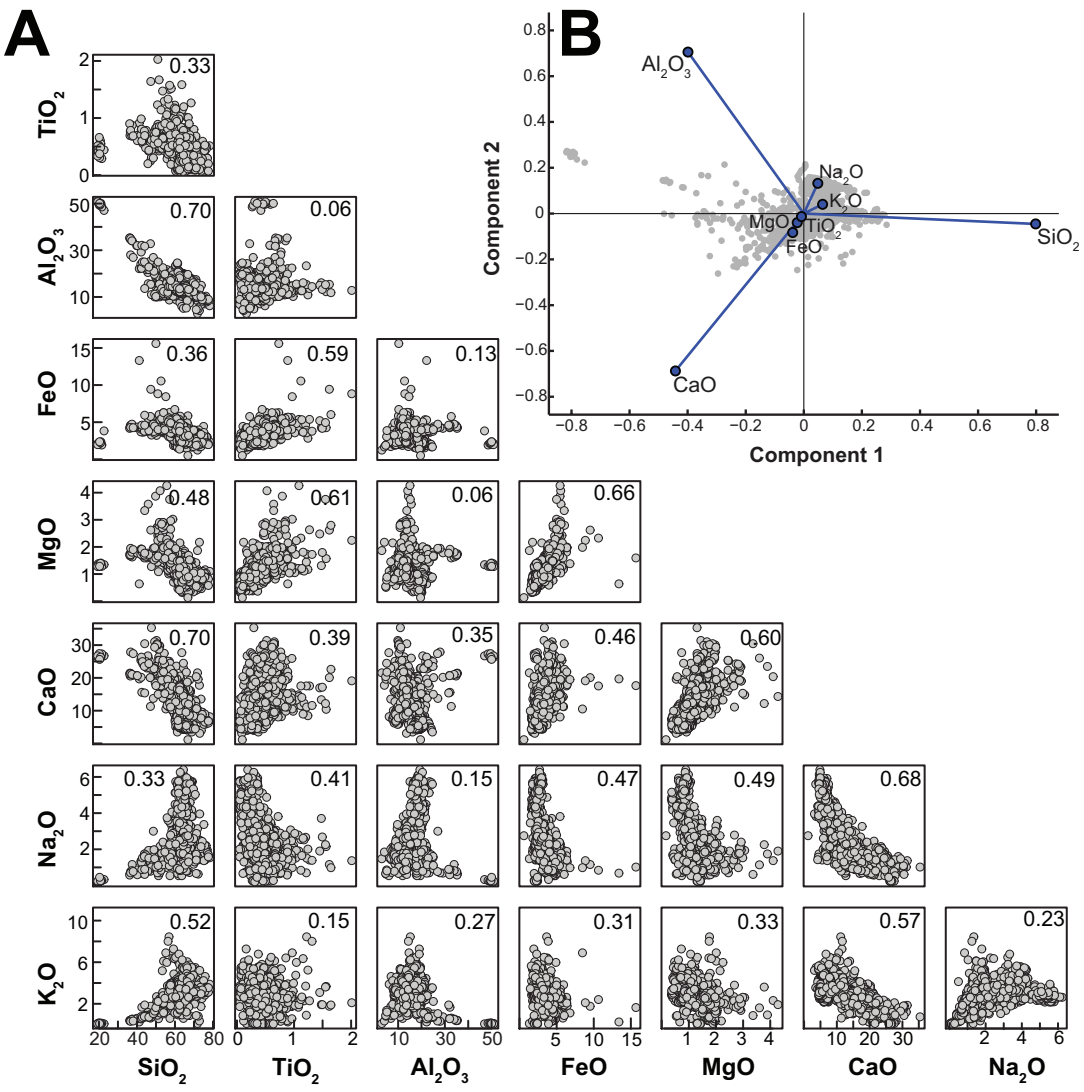

Figure 6

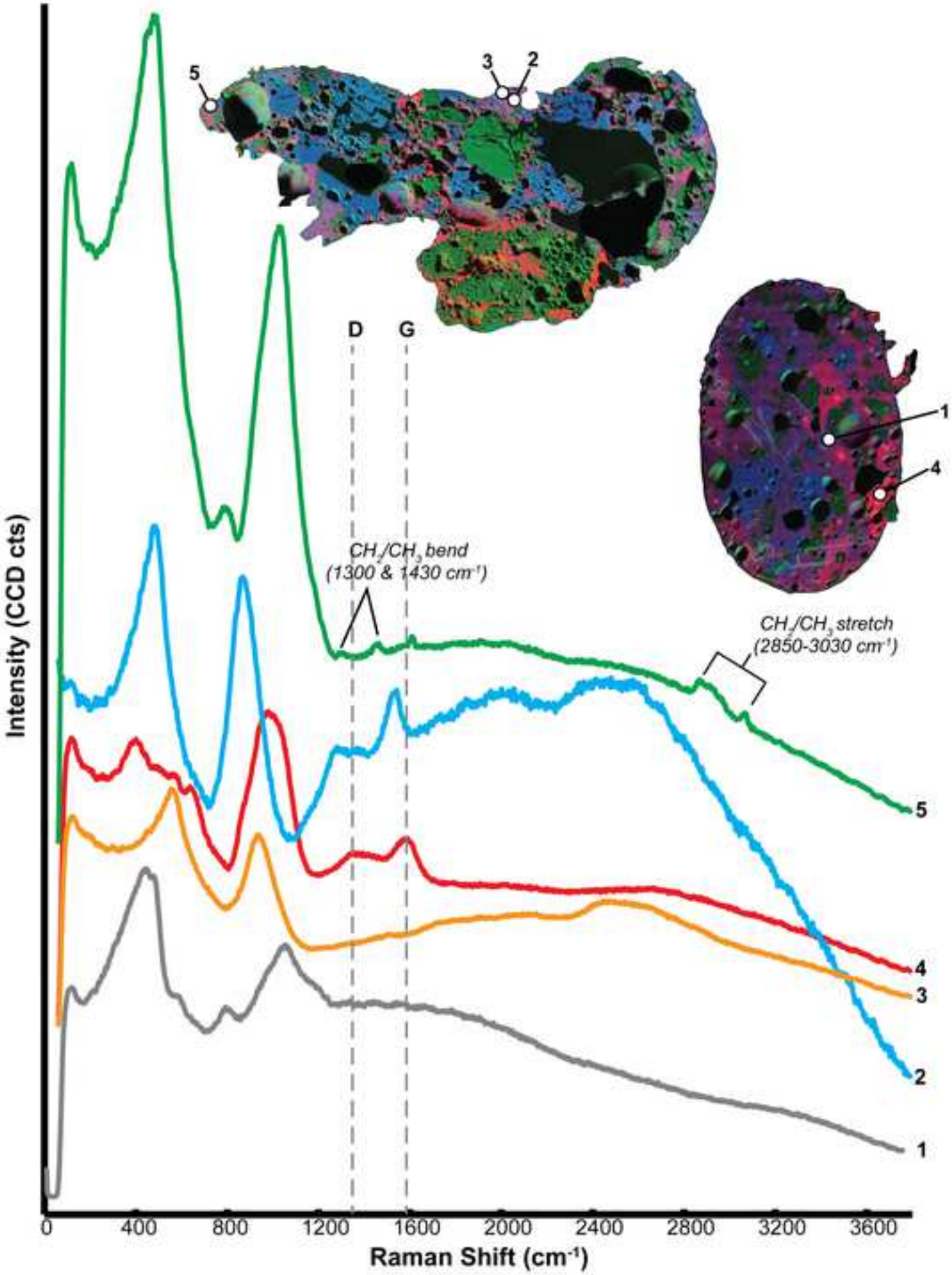

Figure 7

Click here to download Figure Bonamicietal_Fig7.eps

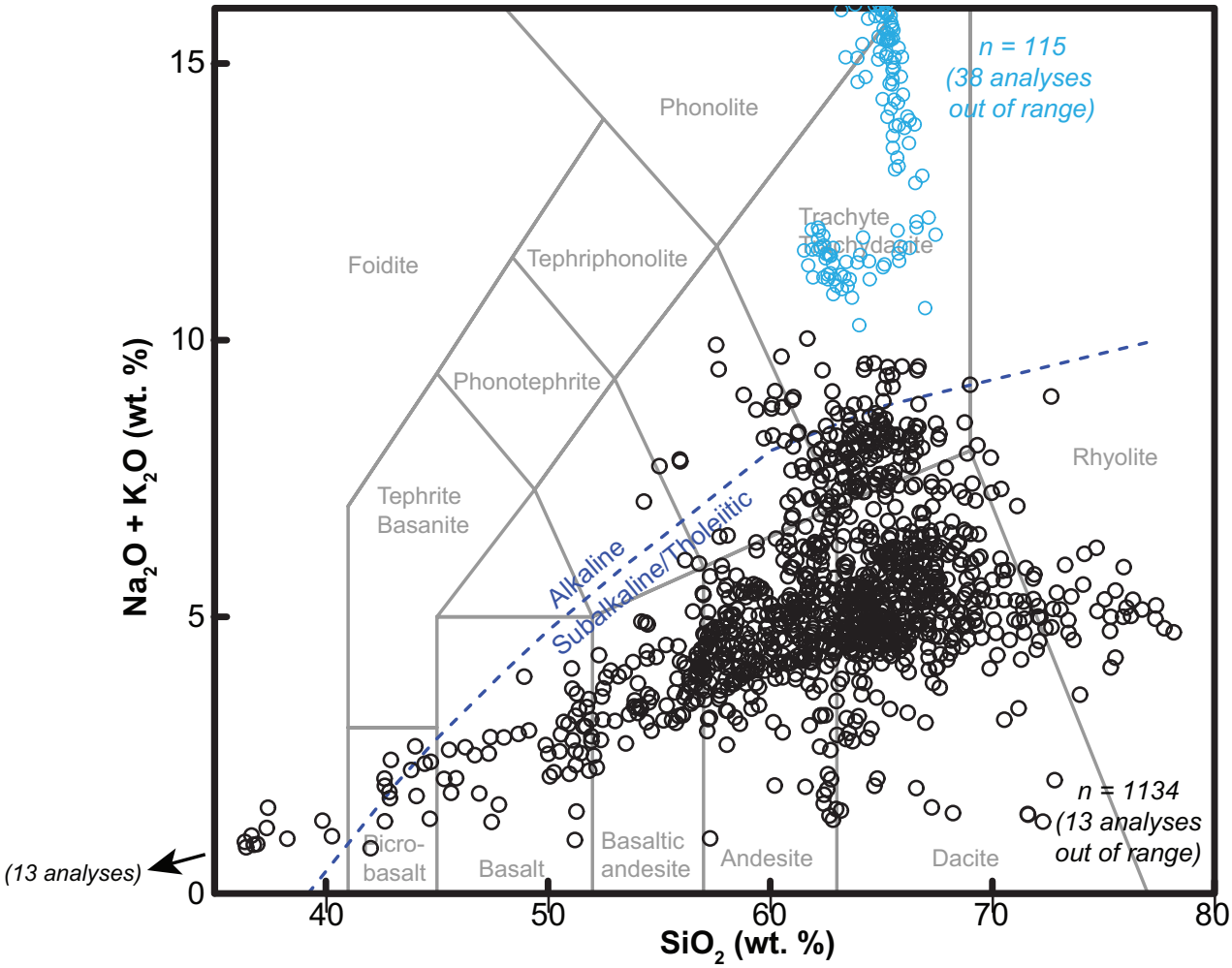

Figure 8

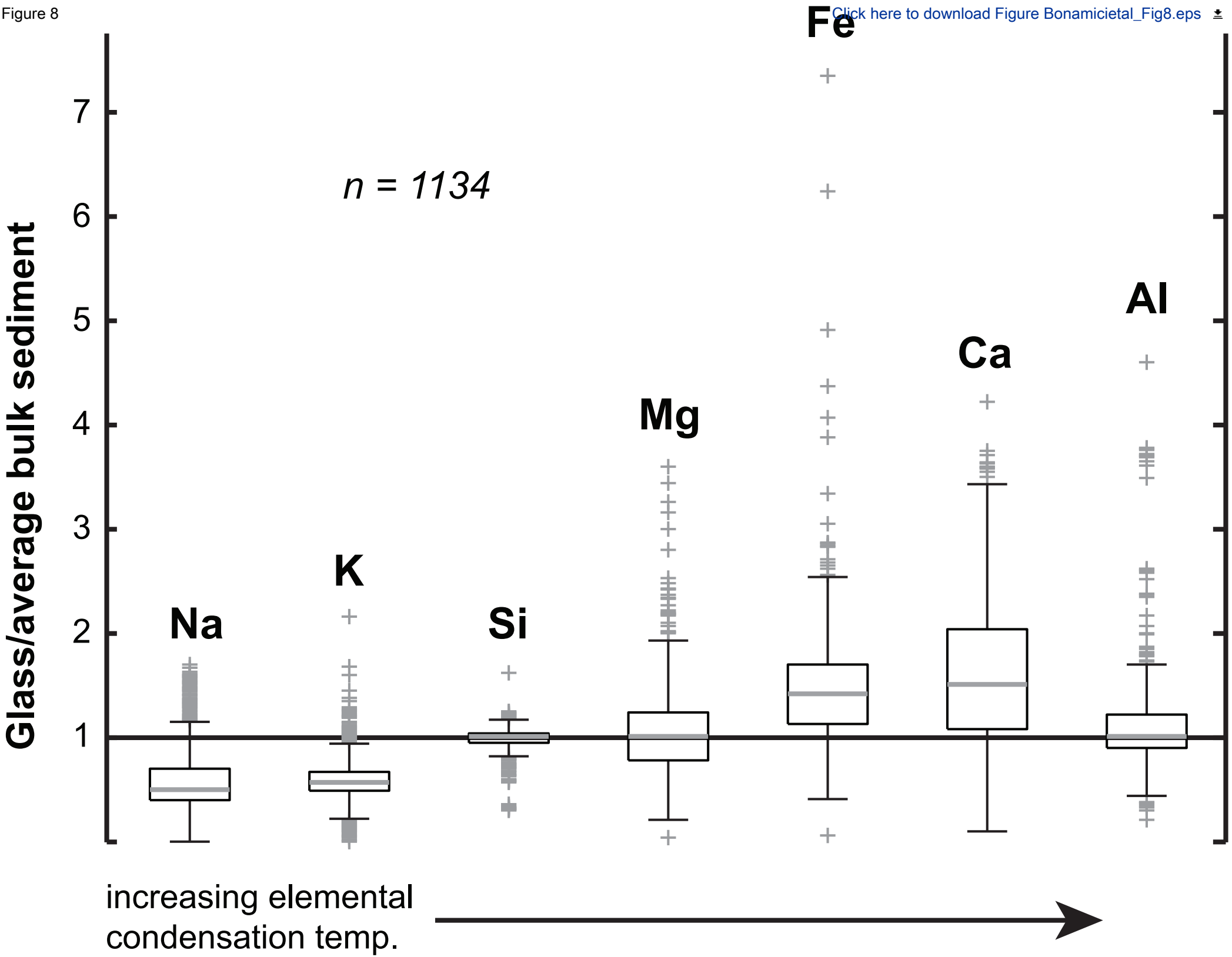

Figure 9

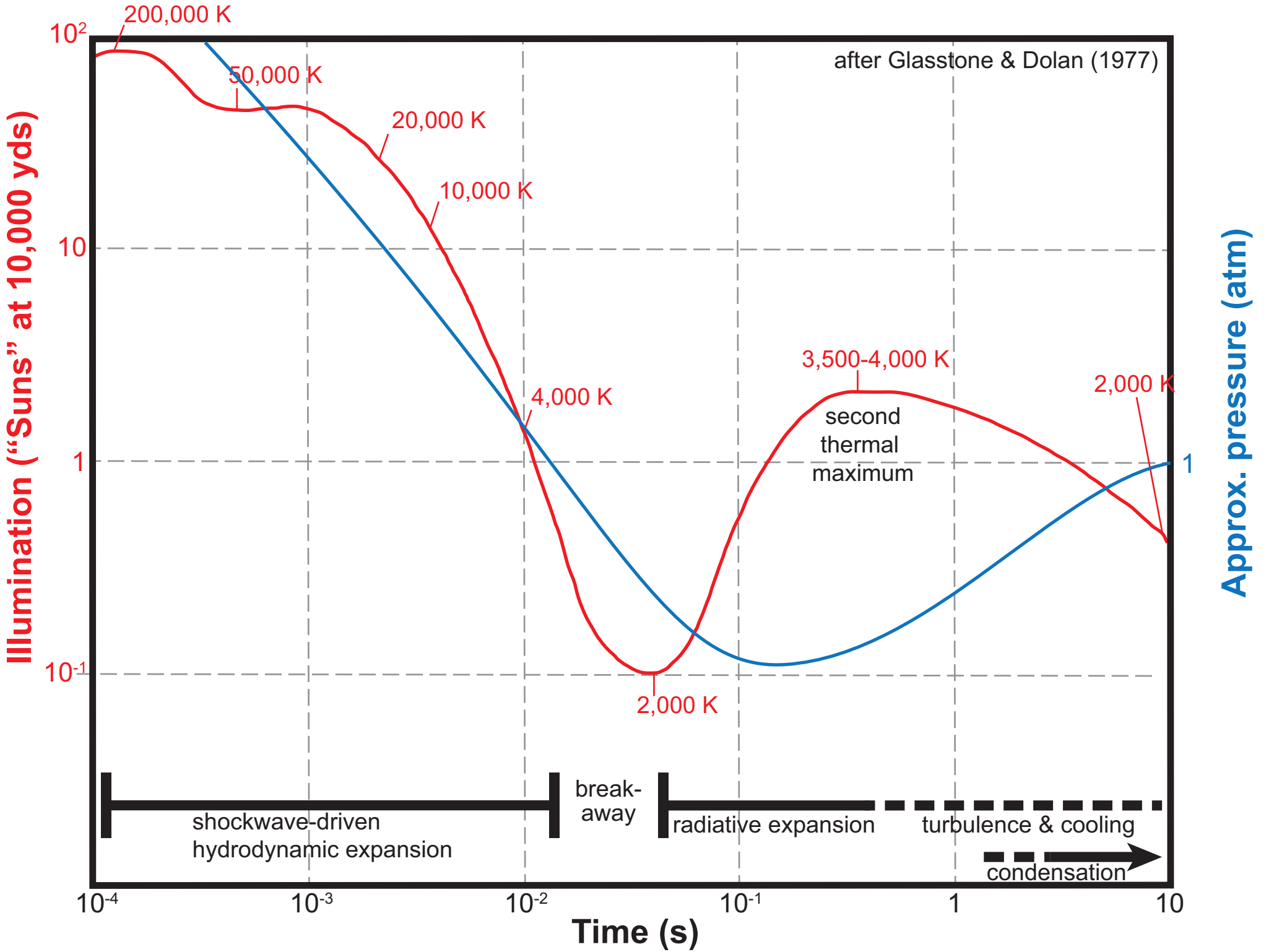

Figure 10

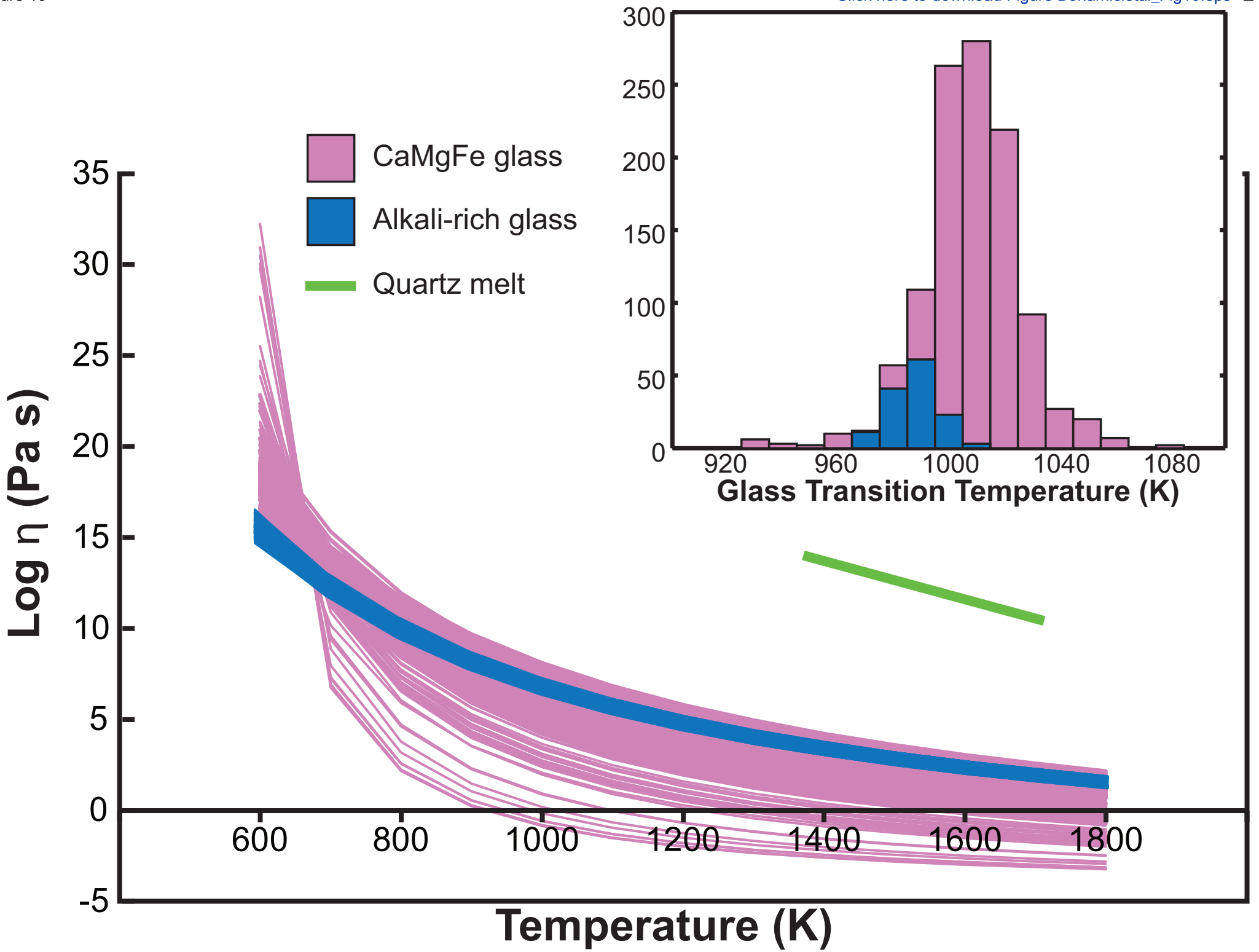

Figure 11

Click here to download Figure Bonamicietal_Fig11.tif

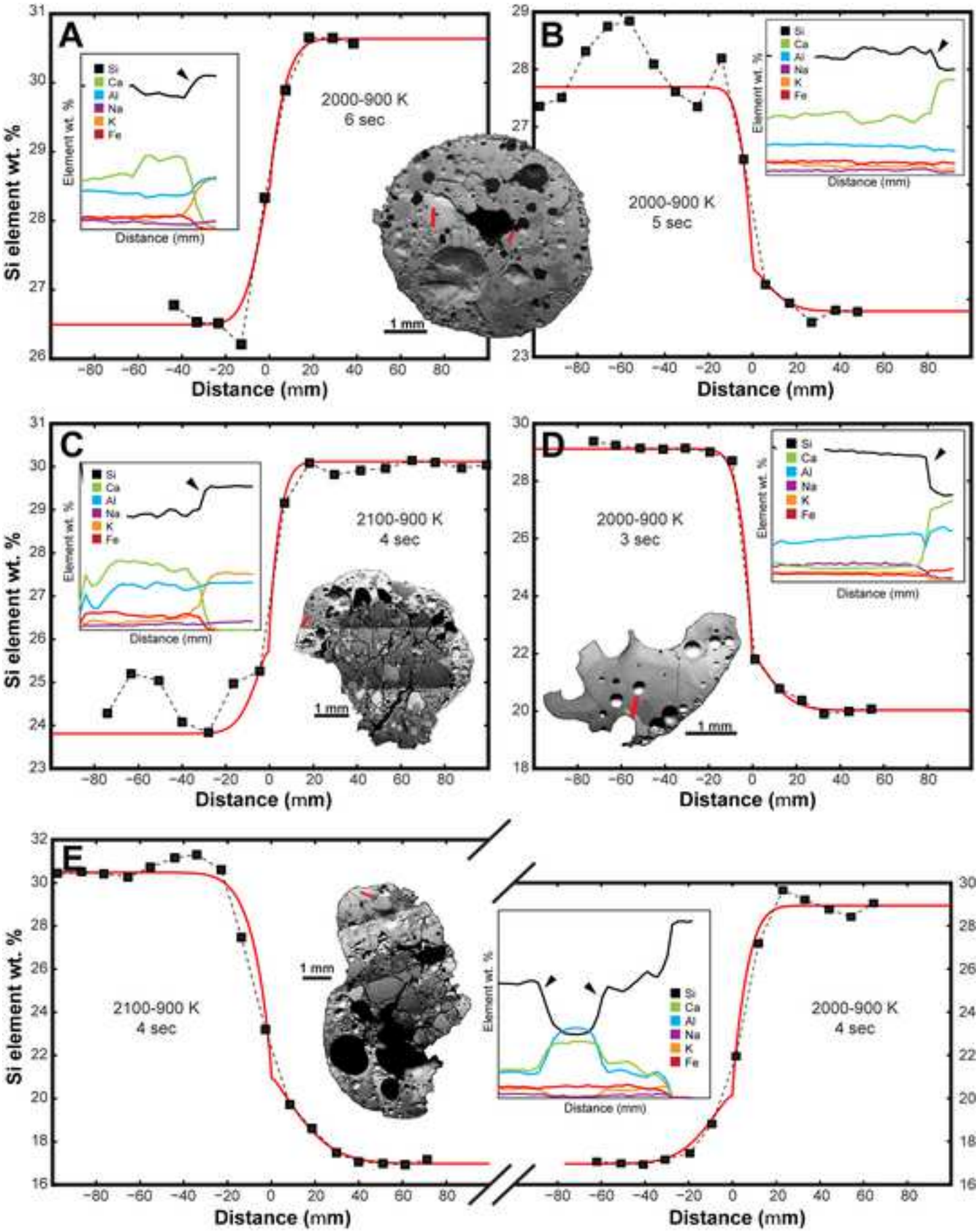

Figure 12

Click here to download Figure Bonamimcietal_Fig12.eps

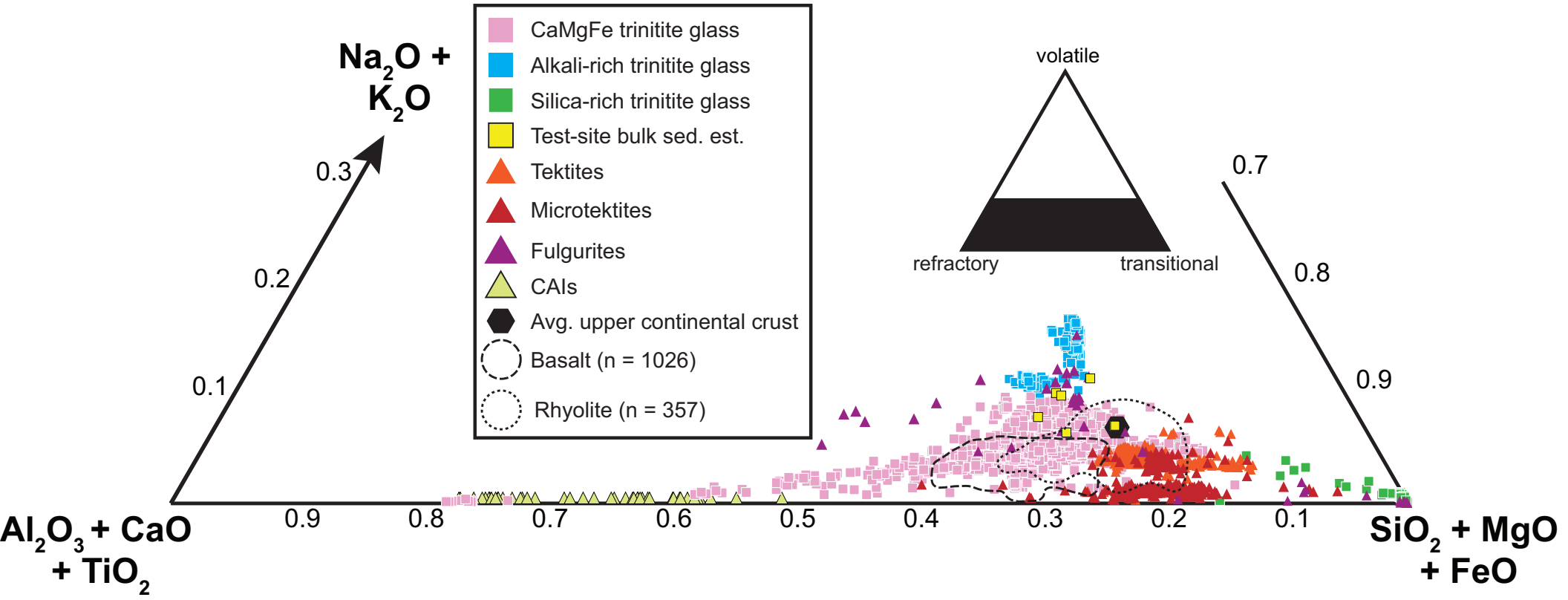

Figure 13

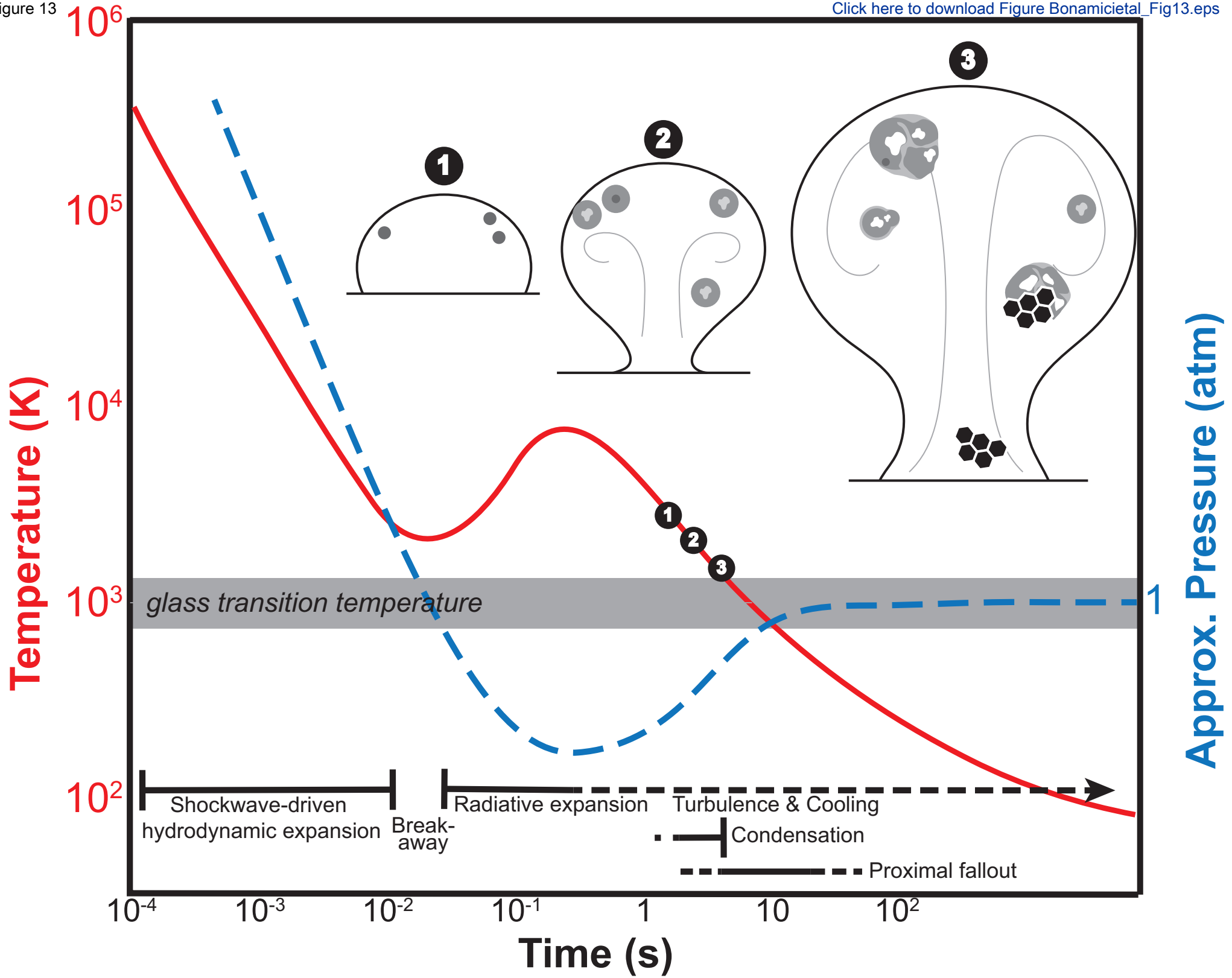

Table 1. Estimated bulk compositions for the Trinity test site sediment.

CALC. BULK SED.[a]	**MINERAL MODES**					**ELEMENT WT. %[b]**								
	Quartz	K-rich alkali fsp	Na-rich plag fsp	Pyroxene[c]	Calcite	Si	K	Na	Al	Ca	Mg	Fe	O	C
High Quartz	0.50	0.15	0.15	0.05	0.15	30.5	3.2	2.3	5.9	5.8	0.9	2.0	48.1	1.3
Low Quartz	0.10	0.35	0.35	0.05	0.15	29.0	4.6	3.3	8.5	4.8	0.5	1.3	47.1	0.8
High K-feldspar	0.30	0.45	0.05	0.05	0.15	29.4	7.3	1.8	7.4	3.7	0.7	1.5	47.2	1.0
High Na-feldspar	0.30	0.05	0.45	0.05	0.15	29.8	0.8	4.0	7.5	6.7	0.7	1.6	47.8	1.0
High Calcite	0.35	0.20	0.10	0.05	0.30	26.3	4.1	1.9	5.6	9.2	0.8	1.9	47.7	2.5
#7 mineral aggregate	0.23	0.32	0.23	0.05	0.18	28.8	4.9	2.8	7.7	5.4	0.6	1.3	47.3	1.1
Minimum[d]	*0.10*	*0.05*	*0.05*	*0.05*	*0.15*	*26.3*	*0.8*	*1.8*	*5.6*	*3.7*	*0.5*	*1.3*	*47.1*	*0.8*
Maximum[d]	*0.50*	*0.45*	*0.45*	*0.05*	*0.30*	*30.5*	*7.3*	*4.0*	*8.5*	*9.2*	*0.9*	*2.0*	*48.1*	*2.5*
Average[e]						*29.0*	*4.1*	*2.7*	*7.1*	*5.9*	*0.7*	*1.6*	*47.5*	*1.3*

[a]Estimated sediment compositions based on observations at the test site (Fig. 1) and descriptions of Jornada del Muerto sediments and Oscura Mountain lithologies. Last composition is from the modal mineralogy measured in a mineral aggregate included within bead #7.

[b]See Appendix for exact calculations to arrive at element wt. % values.

[c]Pyroxene is used as a representative mafic mineral, assumed to contribute equal parts Mg and Fe. Actual mafic mineralogy of the test site sediment may include hornblende, biotite, and/or chlorite. Note that the pyroxene mode was assumed (not measured) for bead #7 due to lack of phase map including Fe or Mg.

[d]Used to plot the upper and lower bounds of the bulk sediment composition shown in Fig. 5 data compilation.

[e]Used to calculated relative element enrichments and depletions plotted in Fig. 9.